Article

A dendritic cell vaccine for both vaccination and neoantigen-reactive T cell preparation for cancer immunotherapy in mice

Qing Li[1,2,7], Hao Zeng[2,7], Ting Liu[2,7], Peipei Wang [2], Rui Zhang[3], Binyan Zhao[3], Tang Feng[2], Yuling Yang[3], Jiumei Wu[4], Yue Zheng[2], Bailing Zhou[3], Yang Shu [5], Heng Xu [3,6], Li Yang [3] ✉ & Zhenyu Ding [2] ✉

Adoptive cell transfer (ACT) using neoantigen-specific T cells is an effective immunotherapeutic strategy. However, the difficult isolation of neoantigen-specific T cells limits the clinical application of ACT. Here, we propose a method to prepare neoantigen-reactive T cells (NRT) for ACT following immunization with a tumor lysate-loaded dendritic cell (DC) vaccine. We show that the DC vaccine not only induces a neoantigen-reactive immune response in lung cancer-bearing mice in vivo, but also facilitate NRT cell preparation in vitro. Adoptive transfer of the NRTs as combinatorial therapy into DC vaccine-immunized, LL/2 tumor-bearing mice allows infiltration of the infused NRTs, as well as the enrichment of neoantigen reactive, non-ACT/NRT T cells into the tumor microenvironment with the function of these neoantigen-reactive T-cell receptors validated in vitro. In summary, we propose a method for preparing NRTs that increases ACT efficacy and paves the way to the design of personalized immunotherapies.

The immune system plays a key role in recognizing and eliminating tumor cells, and therapeutic strategies that utilize the immune system to eliminate tumors have made tremendous advances in recent years[1]. Currently, commonly used tumor immunotherapy strategies include immune checkpoint blockade (CPB)[2,3], adoptive cell transfer (ACT)[4,5], and tumor vaccines[1]. Generally, these therapies treat tumors by activating the body's immune system or abrogating the body's immunosuppression, and T-cell recognition of tumor antigens is crucial for the clinical efficacy of immunotherapy[6].

Tumor neoantigens are proteins produced by mutations in tumor cells that are capable of being processed, presented, and further eliciting specific immune responses[7]. Neoantigen-induced T cells are not affected by central immune tolerance and do not promote the development of autoimmune diseases. Moreover, they have efficient tumor-

killing properties and a suitable safety profile[8,9]. In recent years, an increasing number of studies have confirmed that the activation and amplification of neoantigen-specific T cells are key to the clinical efficacy of CPB treatment[10–14] or adoptive transfusion of tumor-infiltrating lymphocytes (TIL)[15–19]. Neoantigen-specific T cells are the main tumor-killing effector cells. Therefore, screening and expanding T cells that can specifically recognize neoantigens is highly promising for ACT and is one of the frontiers and hotspots in the current research on personalized immunotherapy for tumors[20].

Currently, the commonly used method is to identify neoantigen-specific T cells from TILs, which are subsequently expanded in large numbers before they are reinfused into patients[5]. However, this approach has been successful in only a small proportion of patients with metastatic epithelial cancer[21–25]. The difficulty and low efficiency

[1]Department of Biotherapy, Cancer Center, National Clinical Research Center for Geriatrics, West China Hospital, Sichuan University, Chengdu, China. [2]Department of Biotherapy, Cancer Center, West China Hospital, Sichuan University, Chengdu, China. [3]Department of Biotherapy, Cancer Center and State Key Laboratory of Biotherapy, West China Hospital, Sichuan University, Chengdu, China. [4]Department of Thoracic Surgery, West China Hospital, Sichuan University, Chengdu, China. [5]Gastric Cancer Center, West China Hospital, Sichuan University, Chengdu, Sichuan, China. [6]Department of Laboratory Medicine/Research Centre of Clinical Laboratory Medicine, West China Hospital, Sichuan University, Chengdu, China. [7]These authors contributed equally: Qing Li, Hao Zeng, Ting Liu. ✉e-mail: yl.tracy73@gmail.com; dingzhenyu@scu.edu.cn

of screening neoantigen-specific T cells and the complex and time-consuming preparation of neoantigen-specific T cells for ACT limit its widespread clinical application. Although many studies have been devoted to exploring new ways to screen neoantigen-specific T cells from TILs[26–29] or peripheral blood lymphocytes (PBL)[30–34] for ACT therapy, identifying neoantigen-specific T cells remains challenging.

Studies have shown that neoantigen vaccines induce neoantigen-specific T-cell responses[35–42]. These clinical studies not only demonstrated the great potential of personalized immunotherapy based on neoantigens but also provided novel insights for neoantigen-specific T-cell screening and ACT therapy. We hypothesized that neoantigen-specific T cells could be isolated from PBLs after immunization with neoantigen vaccines[43]. However, in our preliminary clinical studies, we found that the screening of neoantigens, synthesis of peptides and preparation of vaccines were complicated and time-consuming, and some patients with advanced lung cancer died of disease progression during the waiting process[35]. Compared to neoantigen vaccines, tumor lysate vaccines not only are fast and easy to prepare and contain more immunogenic epitopes but also promote and ensure the balanced activation of CD4 + T and CD8 + T cells[44]. More importantly, the use of a tumor lysate vaccine for the treatment of ovarian cancer patients has been found to induce neoantigen-specific T-cell immunity after vaccine immunization[45].

Based on the challenges facing neoantigen-specific T-cell ACT therapy and inspired by the above findings, we propose a research strategy for preparing neoantigen-reactive T cells (NRT) for ACT therapy after immunization with an oxidized tumor lysate-loaded dendritic cell (DC) vaccine. Our preclinical study demonstrates that this DC vaccine triggers a neoantigen-specific immune response and that NRT can be effectively generated by pulsing DCs with immunogenic neoantigens and culturing them with lymphocytes from vaccinated mice. When these NRTs are adoptively transferred into mice already immunized with the vaccine and bearing LL/2 tumors, they mount a more potent antitumor attack. Moreover, infused NRTs are found to home in on the tumor microenvironment, and the vaccine-NRT combo reshapes this environment to impede tumor progression. Our research provides a new and convenient method for preparing NRT for ACT. Clinical translation of this approach has the potential to increase ACT efficacy.

Results

The preparation of a high-quality DC vaccine is feasible

Referring to a previous report[45], we prepared whole-tumor lysates by repeatedly freeze-thawing hypochlorous acid (HOCl)-oxidized LL/2 cells followed by loading the tumor lysates onto DCs to prepare OCDC vaccines (Supplementary Fig. 1). To determine the optimal HOCl concentration leading to LL/2 cell necrosis, we investigated the effects of different HOCl concentrations on LL/2 cell viability (Supplementary Fig. 2). Through Trypan Blue staining and flow cytometry detection of necrotic cells, we found that when the HOCl concentration was 0.9 μM, 98.77% of the cells were PI and Annexin V double-positive (Supplementary Fig. 2); therefore, 0.9 μM HOCl was selected for inducing LL/2 necrosis in subsequent experiments. After 6 cycles of repeated freezing and thawing of oxidized necrotic LL/2 tumor cells, we prepared LL/2 tumor lysates. We induced mouse bone marrow cells to differentiate toward DCs by administering recombinant mouse granulocyte–macrophage colony stimulating factor (rmGM−CSF) and prepared empty-loaded DC vaccines (henceforth referred to as DC vaccines) or OCDC vaccines by not adding or adding HOCl-oxidized LL/2 tumor cell lysates during DC culture. We assessed the quality of the prepared vaccines by flow cytometry detection of DC phenotypic markers. The results showed that the percentage of mature DCs was >90% for both the DC and OCDC vaccines (Supplementary Fig. 3). These results indicated that the OCDC vaccine preparation was feasible and that the OCDC vaccine was of acceptable quality for subsequent experiments.

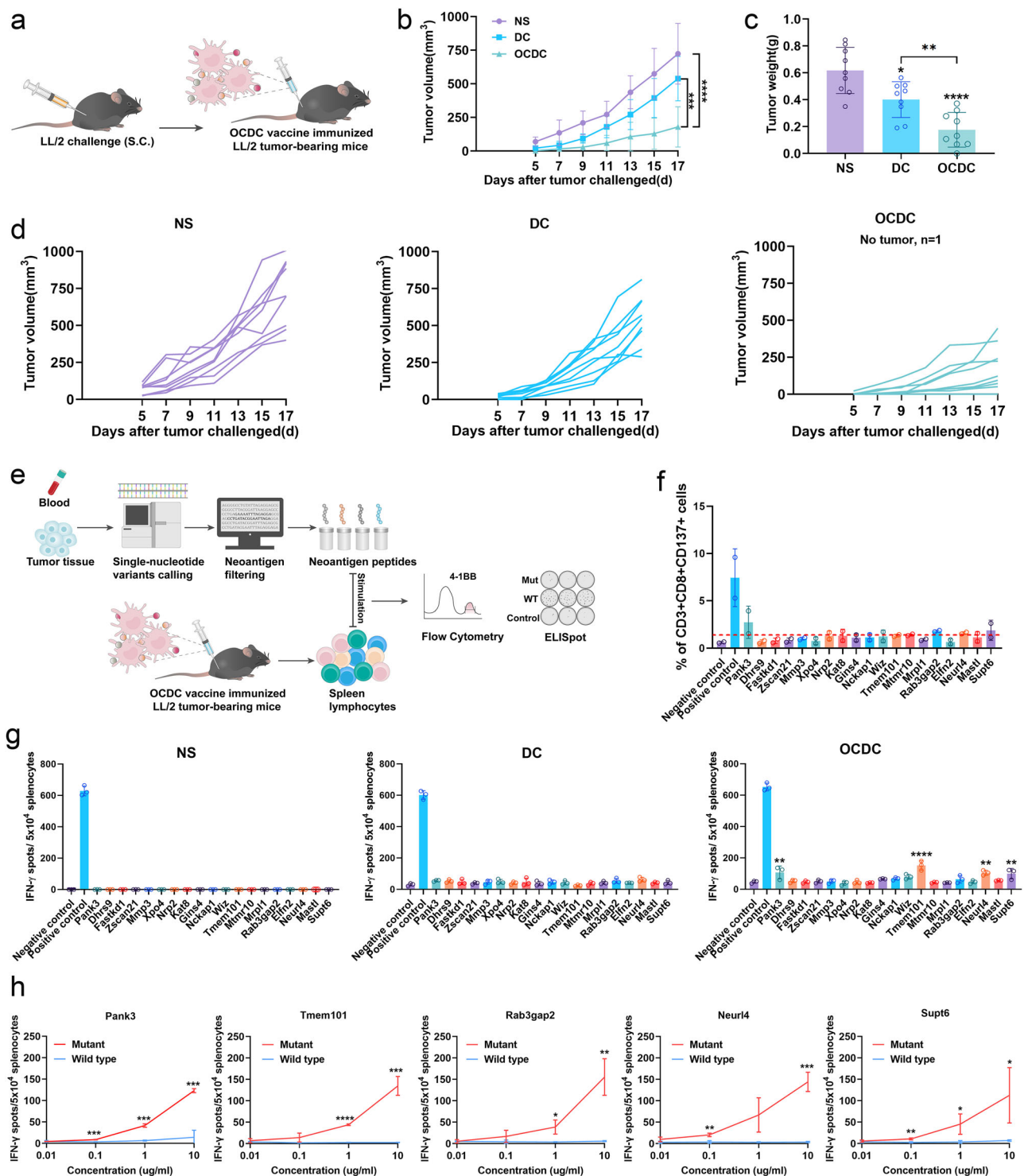### The OCDC vaccine is effective and safe

First, an LL/2 subcutaneous tumor model was established to evaluate the antitumor effect of the OCDC vaccine (Fig. 1a and Supplementary Fig. 4a). Compared with those in the other groups, the tumors in the OCDC group grew at a slower rate and had significantly lower average tumor volume and weight (Fig. 1b–d and Supplementary Fig. 4b). Furthermore, an LL/2 lung metastasis model was established to evaluate the antitumor effect of the OCDC vaccine (Supplementary Fig. 4e). The results showed that the OCDC vaccine also had a greater antitumor effect on the LL/2 lung metastasis model (Supplementary Fig. 4f-h). Hematoxylin and eosin (H&E) staining of lung tissue samples revealed fewer tumors in the OCDC group than in the other groups (Supplementary Fig. 4f). Moreover, by counting the number of tumor nodules on the lung tissue surface and measuring the weight of the lungs, we found that the OCDC vaccine exerted a greater antitumor effect than the DC vaccine (Supplementary Fig. 4g, h). To evaluate the safety of the vaccine, we used H&E and Masson's trichrome staining to detect pathological changes and collagen deposition, respectively. The results showed that the OCDC vaccine produced no obvious toxic side effects on the main organs of the mice (Supplementary Fig. 4c, d, and i).

The OCDC vaccine triggers a neoantigen-specific immune response

We further detected the responses of spleen lymphocytes to different neoantigen peptides by flow cytometry and interferon gamma (IFN-γ)-precoated enzyme-linked immunospot (ELISpot) assays (Fig. 1e). We found that, compared to DCs without neoantigen peptide loading (negative control), DCs loaded with certain neoantigen peptides upregulated the expression of CD137 in CD3 + CD8 + T cells after coculture with spleen lymphocytes from mice immunized with the OCDC vaccine (Fig. 1f and Supplementary Fig. 5). The ELISpot results also showed that the spleen lymphocytes of the mice in the NS group did not respond to any neoantigen peptide (Fig. 1g and Supplementary Fig. 6a). After stimulation with neoantigen peptides, the spleen lymphocytes from mice in the DC group exhibited an increase in IFN-γ secretion, but the difference was not statistically significant compared with that in the splenic lymphocytes not stimulated with any peptide (negative control) (Fig. 1g and Supplementary Fig. 6a). However, in the OCDC cohort, IFN-γ secretion by splenic lymphocytes was significantly increased after stimulation with Pank3, Tmem101, Neurl4, or Supt6 (Fig. 1g and Supplementary Fig. 6a). Considering the above results, we speculated that immunization with the OCDC vaccine induced specific T-cell recognition of the neoantigens Pank3, Tmem101, Rab3gap2, Neurl4, and Supt6. Moreover, we found that the spleen lymphocytes of mice immunized with the OCDC vaccine responded to mutant peptides but not to the corresponding wild-type peptides (Fig. 1h and Supplementary Fig. 6b).

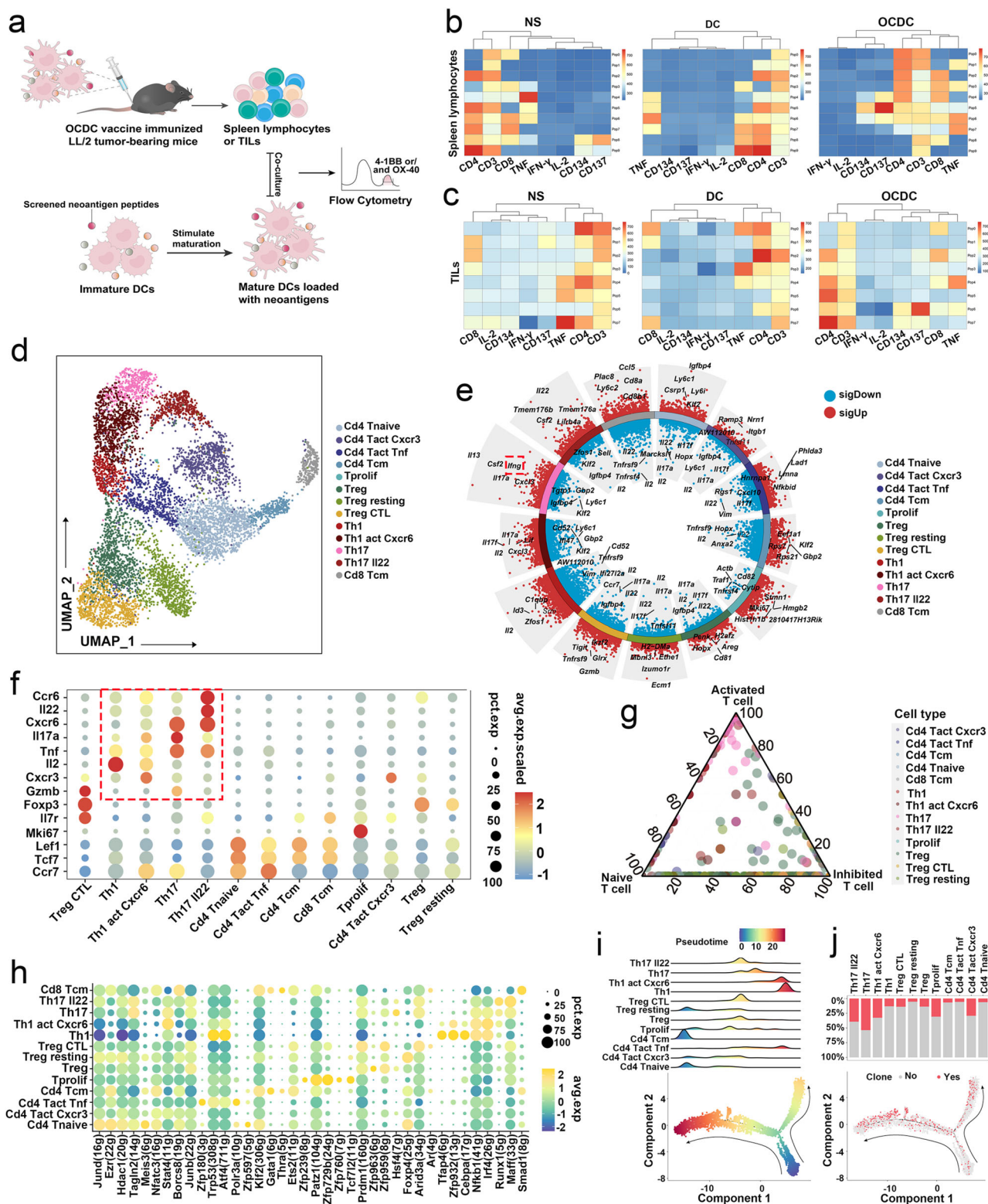### The generation of OCDC vaccine-induced NRTs is feasible

To verify whether these five neoantigens were truly immunogenic, the spleen lymphocytes and TILs of mice in each group were cocultured with DCs loaded with the screened neoantigen peptides for 24 h, and the expression of CD134 and CD137 was determined by flow cytometry (Fig. 2a and Supplementary Fig. 7a). The results showed that the expression of CD134 and CD137 in the spleen lymphocytes and TILs of mice in the OCDC group was significantly increased after coculture with DCs loaded with the screened neoantigen peptides (Fig. 2b, c and Supplementary Fig. 7b−e). Thus, we concluded that the OCDC vaccine could induce a neoantigen-specific immune response in the tumor microenvironment (TME) and splenic lymphocytes and that these five neoantigen peptides were immunogenic peptides. In subsequent experiments, we prepared NRTs by coculturing splenic lymphocytes from mice immunized with the OCDC vaccine with DCs loaded with these five neoantigen peptides.

Fig. 1 | The OCDC vaccine is effective and can trigger neoantigen-specific immune responses. a Experimental design. **b** Mean tumor volume ($n = 9$ independent animals in each group). **c** Tumor weight ($n = 9$ independent animals in each group). **d** Tumor growth curves of individual mice ($n = 9$ independent animals in each group). **e** Schematic representation of the immune response of splenic lymphocytes to neoantigens after immunization with the OCDC vaccine. **f** Proportion of CD3 + CD8 + CD137+ cells in splenic lymphocytes stimulated with mutant peptides after immunization with the OCDC vaccine ($n = 2$ independent experiments). **g** Statistical analysis of the IFN-γ ELISpot assay results for splenic lymphocytes from different groups of mice stimulated with mutant peptides ($n = 3$ biologically independent samples). **h** Statistical analysis of the IFN-γ ELISpot assay results for mouse spleen lymphocytes stimulated with wild-type or mutant peptides ($n = 3$ biologically independent samples). Data were expressed as the mean ± SD (**b**, **c**, **f**, **g** and **h**). Ordinary one-way ANOVA with Tukey's multiple comparisons test (**b**, **c**, **g**) and Unpaired t test (**h**) were carried out for statistical analysis. *$p < 0.05$, **$p < 0.01$, ***$p < 0.001$, and ****$p < 0.0001$. Source data and P values are provided as a Source Data file.

Fig. 2 | Preparing OCDC vaccine-induced neoantigen reactive T cells (NRT) is feasible. a Schematic diagram of the immunogenicity verification of the screened neoantigens. b Flow cytometric results of splenic lymphocytes from each group of mice after coculture with DCs loaded with immunogenic neoantigen peptides ($n = 3$ biologically independent samples). c Flow cytometry results of TILs from each group of mice after coculture with DCs loaded with immunogenic neoantigen peptides ($n = 3$ biologically independent samples). d Uniform manifold approximation and projection (UMAP) plots of flow-sorted CD3 + CD137+ single cells from NRTs. e Circle plot showing the differentially expressed gene (DEG) expression in

each cell cluster. f Dot plots showing the expression of representative genes in each cell cluster. g Triangle diagram showing the results of enrichment analysis for each cell cluster. h Dot plots showing the differentially expressed TFs in each cell cluster. i Pseudotime trajectory analysis of the sorted CD137 + T-cell subclusters. The direction of the inferred pseudotime is indicated by the arrow. j Pseudotime trajectory analysis of the sorted CD137 + T-cell subsets. The proportions of clonal cells in different cell clusters are shown in the bar graphs in the upper part of the figure. The direction of the inferred pseudotime is indicated by the arrow. Source data are provided as a Source Data file.

We performed single-cell RNA sequencing (scRNA-seq) on CD3 + CD137+ cells collected via flow cytometry to characterize the NRTs. According to the differentially expressed genes (DEGs) and representative genes, we divided these sorted cells into 13 clusters (Fig. 2d–f). Among these clusters, T-cell subsets that play important roles in the antitumor immune response, such as helper T cells (Th)17 and Th1 cells, were enriched in functional activation-related genes, such as Ifng, Il2, and Tnf (Fig. 2e, f). Additionally, enrichment analysis revealed that Th1 and Th17 cells were activated (Fig. 2g). To further analyze the upstream signals regulating the development of T-cell subsets, we predicted and analyzed the transcription factors (TFs) regulating each subset via SCENIC. As shown in Fig. 2h, there were significant differences in TF signals among the T-cell subsets with different activation states. Notably, the interferon regulatory factors Irf4 and Nfkb1, which are involved in cytokine regulation, were highly expressed in Th17 and Th1 cell subsets.

Following these results, we studied the potential evolutionary trajectory of CD3 + CD137 + T cells via unsupervised pseudotime analysis. The results suggested that CD3 + CD137 + T cells originated from naive T cells and then split into two branches. The left branch consisted of cells mainly from the Th cell population, and the right branch mainly contained Treg cells (Fig. 2i). There was an increase in clonal amplification over time (Fig. 2I, j). Among Th cells, clonal cells accounted for a large proportion, especially Th17 cells, and more than 50% of the cells were clonal cells (Fig. 2j). These results showed that there were activated functional T cells present in the NRTs. Therefore, NRTs could be successfully generated using this method.

The combination of OCDC vaccination and NRT adoptive transfusion is effective and safe

We further developed an LL/2 subcutaneous model to evaluate the antitumor effect and safety of OCDC vaccination combined with adoptive NRT transfusion (Fig. 3a, b). The results showed that the OCDC vaccine combined with adoptive NRT could significantly inhibit the growth of tumors, and the antitumor effect was greater than that of the OCDC vaccine alone (Fig. 3c–e). Furthermore, the combined treatment improved survival (Fig. 3f) and led to fewer visible and microscopic metastatic nodules in the lungs (Supplementary Fig. 8a and b). However, the combination therapy produced no obvious toxic side effects on the main organs, indicating a suitable safety profile (Supplementary Fig. 9). In addition, we also constructed an LL/2 lung metastasis model to evaluate the efficacy and safety of the OCDC vaccine combined with adoptive transfer of NRTs. The results showed that in the lung metastasis model, the combination of the OCDC vaccine with adoptive transfer of NRTs was also effective and safe (Supplementary Fig. 8c, d and Supplementary Fig. 10).

The combination of OCDC vaccination and NRT adoptive transfusion works in other cell line model

To validate whether the OCDC vaccine can elicit neoantigen-specific immune response in other tumor models, we established the CT26 subcutaneous tumor model and the B16 subcutaneous tumor model. Using Trypan Blue staining and flow cytometry to detect the proportion of necrotic cells, we determined the HOCl concentration for oxidizing CT26 and B16 cells to be 0.6 μM and 0.5 μM, respectively (Supplementary Fig. 11). Subsequently, we prepared the OCDC vaccine and immunized tumor-bearing mice. After vaccination, by detecting the response of splenic lymphocytes to neoantigens, we found that the splenic lymphocytes of mice in the OCDC group showed an immune response to the mutant neoantigen peptides (Supplementary Fig. 12). It is noteworthy that in these two models, we have used the immunogenic neoantigens E2f8 and Kif18b, which have been validated in previous literature[46,47]. In the CT26 and B16 models, we further explored the therapeutic efficacy and safety of the OCDC vaccine combined with NRTs. The results showed that in both the CT26 and

B16 models, the combination of the OCDC vaccine with the adoptive transfer of NRTs had good antitumor effects and safety (Supplementary Fig. 13, Supplementary Fig. 14, Supplementary Fig. 15 and Supplementary Fig. 16).

The infused T cells can reach the TME

To verify whether the infused T cells can reach the TME, we established an LL/2 subcutaneous tumor model and prepared T cells from the splenocytes of B6-G/R mice that express green fluorescent protein (GFP) throughout their bodies for adoptive transfer (Supplementary Fig. 17a). After immunizing tumor-bearing B6-G/R mice with the OCDC vaccine, we obtained splenocytes from these mice to prepare adoptively transferred cells. Flow cytometry confirmed that most of the infused lymphocytes were GFP-positive cells (Supplementary Fig. 17b, c).

Seven days after the infusion of T cells, we examined the splenocytes and TME by flow cytometry. We detected GFP-positive T cells in the splenocytes and TME of mice in the OCDC + T and OCDC + NRT groups (Supplementary Fig. 18a, b, d, e). Although the proportion was small, most of these T cells were IFN-γ positive cells (Supplementary Fig. 18c, f). To test whether the infused T cells persisted, we conducted the test again on day 10 post-adoptive transfer. We found that GFP-positive T cells were still detectable in the splenic lymphocytes and the TME of mice in both the OCDC + T and OCDC + NRT groups (Fig. 3g–i and Supplementary Fig. 18g, i), and these GFP-positive cells still exhibited IFN-γ secretion (Fig. 3j, k and Supplementary Fig. 11h). Interestingly, we can distinguish NRTs from other T cells in TILs using flow cytometry and multiplex fluorescence immunohistochemistry (Fig. 3i, and Supplementary Fig. 18j), and what is more interesting is that we found that the secretion of IFN-γ in GFP-negative T cells in the OCDC + NRT group is also significantly increased compared to the other groups (Fig. 3l, m). Therefore, it is necessary to explore the changes in the TME following the administration of OCDC vaccines in combination with NRTs infusion.

Single-cell analysis reveals the transcriptomic landscape of the TME in the LL/2 tumor model

To better understand the effect of OCDC vaccination combined with NRT adoptive transfusion on the TME, we applied scRNA-seq to characterize the transcriptome of immune cells as well as tumor cells in the LL/2 subcutaneous tumor model (Supplementary Fig. 19a). After quality control, 48447 single cells were clustered into 7 major clusters. The following classic marker genes were used to annotate the major cell types in each cluster: T/NK cells (Cd3d, Nkg7); macrophages/monocytes (Cd68, C1qb); DCs (Flt3); neutrophils (Csf3r); endothelial cells (Cdh5); and fibroblasts (Col1a1) (Supplementary Fig. 19b, c). There was extensive copy number variant (CNV) in tumor cells compared with normal immune cells (T cells, B cells, etc.) (Supplementary Fig. 19d). The average number and proportional distribution of major cell types in each group are shown in Supplementary Fig. 19e. We also detected an elevated number of T/NK cells in the OCDC + NRT group compared to the other groups (Supplementary Fig. 19f). Further analysis revealed that different cell types were regulated by different TFs, with cancer cells, macrophage/monocyte cells, and T/NK cells showing highly specific transcriptional regulation, suggesting that they were regulated by unique TFs (Supplementary Fig. 19g).

OCDC vaccination combined with NRT adoptive transfusion boosts antitumor T cells and reduces immunosuppressive T cells

To better characterize the TILs in each group, we analyzed the T/NK population and identified 15 distinct clusters (Fig. 4a and Supplementary Fig. 20a). Cluster stability was supported by distinct signature genes (Fig. 4b and Supplementary Fig. 20b). The distributions of these clusters were highly heterogeneous among the different treatment groups (Fig. 4c, d and Supplementary Fig. 20c). In particular, the
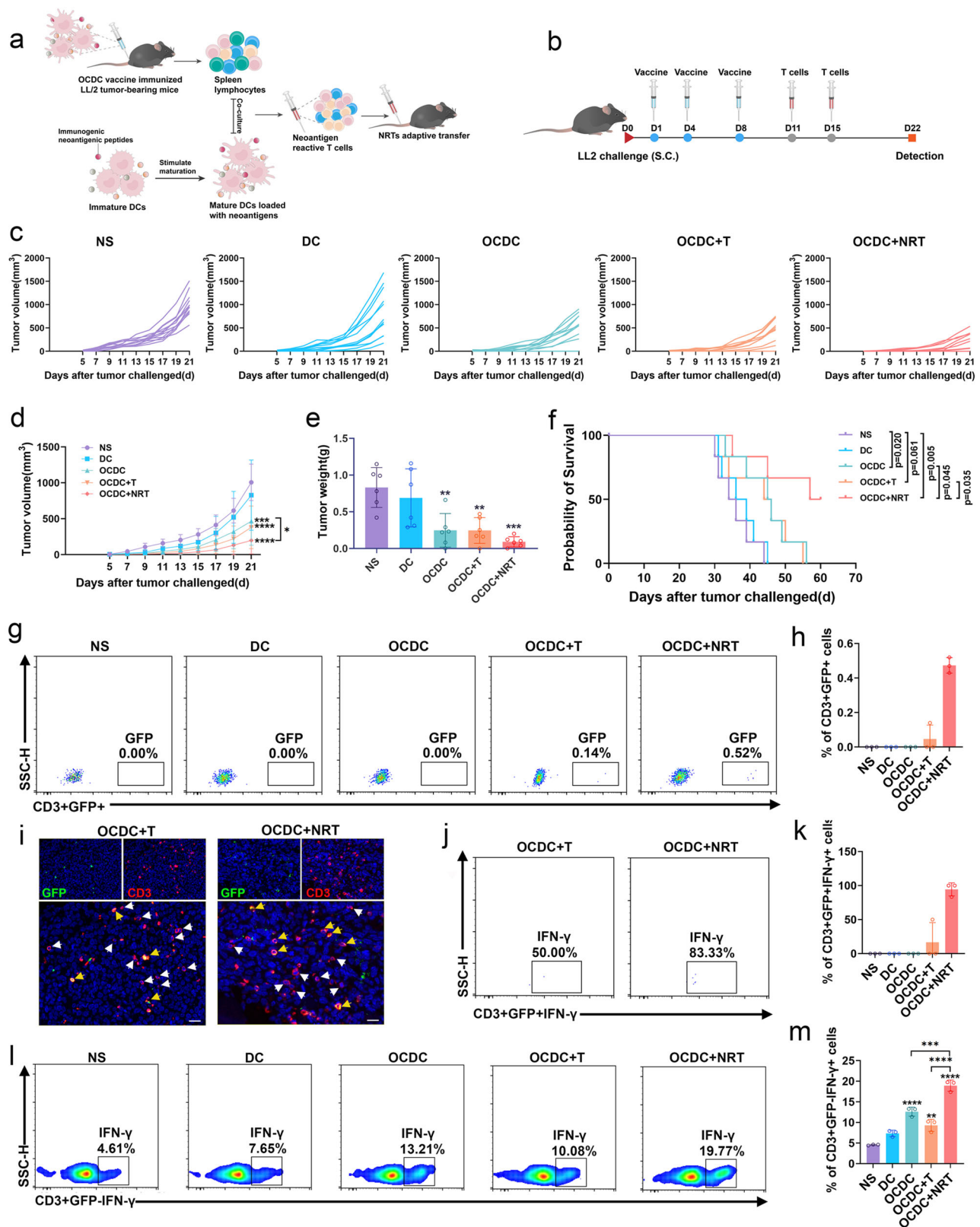
OCDC + NRT group was enriched in Th1 cells (CD4-Cxcr3/Cxcr6-Th1), effector memory T (Tem) cells (CD8-Gzmk-Tem), effector T (Teff) cells (CD8-Gzmk/Gzma-Teff) and tanergic T cells (CD4-Tnfsf8-T tanergy), whereas Treg cells (CD4-Foxp3-Treg) were relatively rare (Fig. 4c, d and Supplementary Fig. 20c).

We studied the potential evolutionary trajectory of CD8 + T cells via unsupervised pseudotime analysis. The trajectory originated from naive T cells and split into two branches (Fig. 4e). The upper branch exhibited a transitional phase with a mixture of Teff, Tem and dysfunctional T cells before reaching a completely exhausted phenotype (Fig. 4e). The lower branch consisted of cells mainly from the effector cell population (Fig. 4e). Consistently, T cells in the OCDC + NRT group developed along the trajectory and exhibited an increase in Teff and Tem cells (Fig. 4f). In CD8 + T cells, the expression of naive cell

Fig. 3 | Antitumor effects of OCDC vaccination combined with NRT adoptive transfusion. a Experimental design. **b** Schematic of the vaccine immunization and T-cell infusion time points. **c** Tumor growth curves of individual mice ($n = 12$ independent animals in each group). **d** Mean tumor volume ($n = 12$ independent animals in each group). **e** Tumor weight ($n = 6$ independent animals in each group). **f** Survival curves ($n = 6$ independent animals in each group). **g** Representative images showing the proportion of GFP + T cells in tumor tissues of each group ($n = 3$ biologically independent samples). **h** Statistical results of the proportion of GFP + T cells in tumor tissues of each group ($n = 3$ biologically independent samples). **i** Multi-fluorescence immunohistochemistry shows the GFP-positive T cells and GFP-negative T cells in OCDC + T group and OCDC + NRT group ($n = 3–4$ independent fields of view from two independent experiments; where the yellow arrows represent GFP-positive T cells, and the white arrows represent other T cells

in the tumor microenvironment; scale bar, 20 μm). **j** Representative images showing the proportion of GFP + IFN-γ + T cells in tumor tissues of the OCDC + T group and OCDC + NRT group ($n = 3$ biologically independent samples). **k** Statistical results of the proportion of GFP + IFN-γ + T cells in tumor tissues of each group ($n = 3$ biologically independent samples). **l** Representative images showing the proportion of GFP-IFN-γ + T cells in tumor tissues of each group ($n = 3$ biologically independent samples). **m** Statistical results of the proportion of GFP-IFN-γ + T cells in tumor tissues of each group ($n = 3$ biologically independent samples). Data were expressed as the mean ± SD (**d**, **e**, **h**, **k**, and **m**) and Kaplan-Meier plot (**f**). Unpaired t test (**d**), Ordinary one-way ANOVA with Tukey's multiple comparisons test (**e**, **m**) and Log-rank (Mantel-Cox) test (**f**) were used for statistical analysis. *$p < 0.05$, **$p < 0.01$, ***$p < 0.001$ and ****$p < 0.0001$. Source data and P values are provided as a Source Data file.

characteristic genes (Lef1, Ccr7, Sell, etc.) was gradually down-regulated, while the expression of cytotoxicity-related genes (Gzma, Gzmb, Ifng, etc.) was gradually increased (Fig. 4g, h). At the end of the branch, several exhaustion-related genes (Pdcd1, Lgals3, etc.) were highly expressed (Fig. 4g, h). Gene Ontology (GO) enrichment analysis revealed that these genes in the OCDC + NRT group were specific and enriched in pathways related to T-cell activation and cytotoxicity compared with those in the NS group and the group receiving other treatments, indicating that treatment with the OCDC vaccine combined with NRT adoptive transfusion was unique from other treatments and correlated with the role of T cells (Fig. 4i).

To confirm the results of the scRNA-seq analysis, we applied immunofluorescence and flow cytometry to stain representative markers at the protein level. Multiplex immunofluorescence staining revealed increased T-cell infiltration in the TME of the OCDC + NRT group (Fig. 4j and Supplementary Fig. 20d). The flow cytometry results were generally consistent with the scRNA-seq results, in which there was an increase in cytotoxic lymphocyte (CTL) and memory T-cell proportions and a decrease in the proportion of Treg cells in the TME in the OCDC + NRT cohort (Fig. 4k, l and Supplementary Fig. 20e-h). These results suggested that OCDC vaccination combined with adoptive NRT transfusion could reshape the TME to favor antitumor functions by increasing Teff cell and Tem cell numbers and decreasing immunosuppressive T-cell numbers.

Neoantigen-specific T cells are enriched in the TME of the OCDC + NRT cohort
By analyzing the immune repertoire (IR) in the TME of each group, we found that the abundance and homogeneity of T-cell receptors (TCRs) were reduced in the OCDC + NRT cohort, whereas the diversity and clonal diversity of TCRs were increased (Fig. 5a). Further analysis revealed that the distribution and correlation of TCRs significantly differed between the different groups (Fig. 5b, c). In the OCDC + NRT cohort, TCRs were derived mainly from Th1 cells, CD8+ Teff cells, and CD8+ Tem cells, whereas in the DC subgroup, despite the greater number of TCRs, they were derived mainly from Treg cells, naive T cells and exhausted T cells (Fig. 5b). In the OCDC + NRT cohort, the correlation of TCRs among T-cell subsets was significantly stronger than that in the other groups, and the correlation of TCRs mainly existed among Th1, CD8+ Teff, and CD8+ Tem cells (Fig. 5c).

To determine whether the clonally expanded T cells contained neoantigen-specific T cells and whether the neoantigen-specific T cells were derived from the NRT infusion, we performed single-cell TCR sequencing (scTCR-seq) on single-cell suspensions of tumor tissues from each group and on CD3 + CD137 + T cells sorted from the NRTs (Fig. 5d). Neoantigen-specific T cells were identified by a series of criteria (Fig. 5e). In brief, CDR3β sequences were obtained from CD137 + T cells and TILs, and an overview of these TCRs is shown in Fig. 5f. We noted that some TCR groups were organized into distinct communities through shared CDR3β sequences (Fig. 5g). We further

identified IFN-γ-positive CDR3β sequences that were present in both the sorted CD137 + T cells and the TILs (Fig. 5h, i). We hypothesized that T cells undergo clonal expansion after neoantigen recognition. Finally, after stepwise filtering, we found 6 neoantigen-specific TCRs, four of which were present in the OCDC + NRT cohort (Fig. 5j, k). We visualized the tightly connected neoantigen-specific TCR groups as well as the clusters and found that their sequences were in high agreement and that they all had the vβ31 gene (Fig. 5j, k). These neoantigen-specific TCR groups were also shown to have a strong affinity for immunogenic neoantigen peptides (Supplementary Fig. 21a).

Like the results of scRNA-seq, flow cytometry detection of T cells in the TME revealed more neoantigen-specific T cells in the OCDC + NRT cohort (Supplementary Figs. 21b and c). Thus, we demonstrated that neoantigen-specific T cells were indeed enriched in the TME after NRTs infusion. Flow cytometry also revealed increased expression levels of activating factors in these neoantigen-specific T cells, indicating that these neoantigen-specific T cells were functional (Supplementary Figs. 21d, e). Therefore, we concluded that the OCDC vaccine combined with adoptive NRT could enhance the interaction between T cells, and that neoantigen-specific T cells from infused NRTs could migrate into the TME and these neoantigen-specific T cells were also functional.

Neoantigen-specific TCRs have specific modes and can be activated by neoantigen peptides in vitro
To further characterize neoantigen-specific T cells in vitro, we reflected neoantigen-specific CDR3β sequences to sorted CD137 + T cells (Fig. 6a). We found that these neoantigen-specific TCRs were mainly distributed in superclusters (Fig. 6b) and had shared CDR3β sequences (Fig. 6c). We then identified IFN-γ-positive neoantigen TCRs (Fig. 6d), which were highly concentrated (Fig. 6e). Subsequently, we studied these neoantigen-specific TCRs and found that their sequences were highly consistent and that the Vβ31 gene was used most frequently, suggesting that the Vβ31 gene plays a contributing role in neoantigen recognition (Fig. 6e). These neoantigen-specific TCRs were also shown to have strong affinity for immunogenic neoantigen peptides (Supplementary Fig. 21f). We found that T cells expressing neoantigen-specific TCRs were predominantly activated T cells and were absent from naive T cells (Fig. 6f, g). DEG analysis also revealed that these T cells expressed the activation signature Ifng (Fig. 6h). The enrichment analysis results also revealed that these neoantigen-specific TCRs were indeed present in activated T cells (Fig. 6i). Thus, we demonstrated that these neoantigen-specific TCRs have defined characteristics and can be activated by neoantigen peptides in vitro.

Neoantigen-specific TCR-T cells can specifically identify and perform specific cytotoxic effects on tumor cells
To validate the specific identification and reactivity of the neoantigen-specific TCRs to neoantigens, we filtered three neoantigen-specific
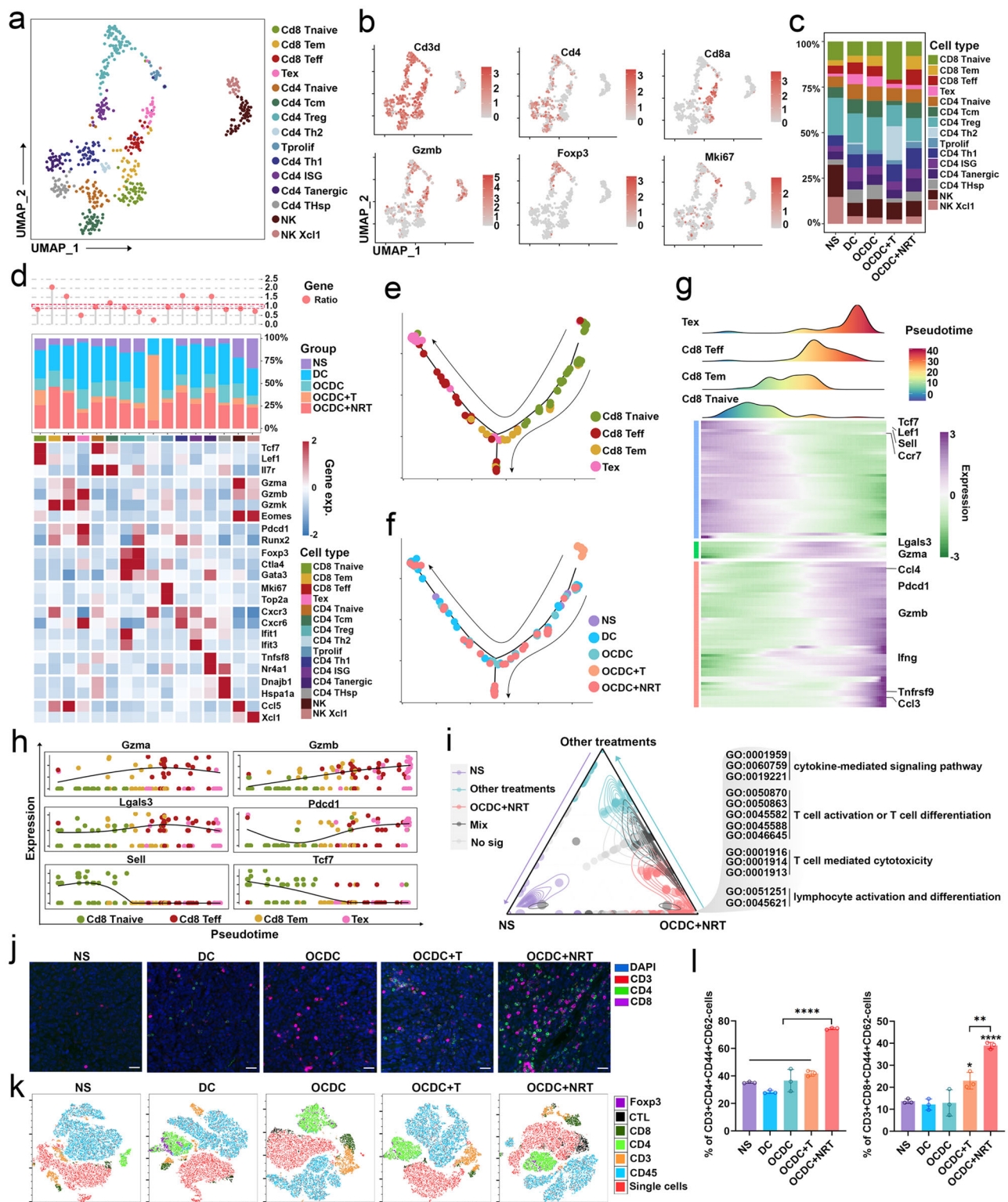
CDR3β sequences of Vβ31 CAWSLGGQDTQYF, Vβ12-2 CASG-DASNQDTQYF, and Vβ3 CASSLGGQDTQYF according to the expression frequency and IFN-γ expression. Neo TCR-T1, Neo TCR-T2, and Neo TCR-T3 were generated from mice lymphocytes by lentiviral transduction of the TCR genes (Fig. 7a). Staining of TCR-T cells using H-2Kb Tetramer-APC carrying five neoantigens suggested that neoantigen-recognizing TCRs were highly expressed in CD4 or CD8 positive neoantigen-specific TCR-T cells (Fig. 7b, c). After co-culturing neoantigen-specific TCR-T cells with LL/2 cells or CT26 cells for 24 h,

LL/2 cells underwent significant early apoptosis and late apoptosis compared with the control and CT26 cells (Fig. 7d). Real-time cell monitors assay revealed that neoantigen-specific TCR-T cells had specific cytotoxic reaction on LL/2 cells, showing a significant difference with uninfected T cells as time increased (Fig. 7e). T cells were collected after 48 h of co-culture with target cells and stained with H2Kb Tetramer-APC carrying Neurl4 peptide and anti-mouse IFN-γ antibody. Compared with the control groups, the specific TCRs were expressed in CD4 or CD8 positive TCR-T cells, most significantly in Neo

Fig. 4 | Response of TILs to distinct treatments. a UMAP plots of T/NK cells, colored by cell type. **b** UMAP plots showing marker gene expression for cell type identification. The legend shows a color gradient of normalized expression. **c** Proportions of each cell type in each group, colored by cell type. **d** Heatmap of fifteen T/NK cell clusters with classical marker genes (bottom), the proportion of each cell subpopulation in each group (middle) and the ratio of the proportion of cells in the OCDC + NRT group to the proportion of cells in the other groups (top). **e** Pseudotime trajectory analysis of the CD8 + T-cell subclusters, colored by cell type. The direction of the inferred pseudotime is indicated by the arrow. **f** Pseudotime trajectory analysis of the sorted CD8 + T-cell subclusters, colored according to different groups. The direction of the inferred pseudotime is indicated by the arrow. **g** Heatmap showing the dynamic expression and clustering of marker genes associated with CD8 + T-cell subclusters over pseudotime. **h** Dot plots showing the dynamic expression of representative genes of CD8 + T-cell subclusters over pseudotime. **i** Gene Ontology (GO) enrichment analysis of T-cell functional pathway expression across treatments. **j** Representative images of tumor tissues from each group stained by multiplex immunofluorescence staining ($n = 8-10$ independent fields of view from three independent experiments; Scale bars represent 20 μm). **k** T-SNE plots showing the flow cytometry results for each group ($n = 3$ biologically independent samples). **l** The number of effective memory T cells (Tem) among the CD4+ and CD8 + T cells in the TIL population ($n = 3$ biologically independent samples). Data were expressed as the mean ± SD (**l**). Ordinary one-way ANOVA with Tukey's multiple comparisons test (**l**) was used for statistical analysis. *$p < 0.05$, **$p < 0.01$, and ****$p < 0.0001$. Source data and *P* values are provided as a Source Data file.

TCR-T1 and Neo TCR-T3 cells (Fig. 7f, g), while more IFN-γ expression was also detected in these two types of TCR-T cells (Fig. 7h, i). We concluded that neoantigen-specific TCR-T cells were able to specifically identify neoantigens and perform specific cytotoxic effects on tumor cells.

OCDC vaccination combined with adoptive NRT transfusion activates DCs and M1-like macrophages

Myeloid cells play an important role in shaping the TME. We analyzed the myeloid cells in our samples and identified 16 subclusters exhibiting distinct patterns of gene expression (Fig. 8a, b). Analysis of the relative proportions of each subcluster across the different groups revealed that Nr4a1+ and H2-Eb1+ macrophages were specifically enriched in the OCDC + NRT cohort, while Mcm3+ macrophages were less abundant (Fig. 8c). By analyzing DC subclusters, we found that the OCDC + NRT group had more activated DCs (Fig. 8d, e). Using the CellChat ligand–receptor complex database, we next assessed the cellular crosstalk between DCs and different cell types among the different groups by analyzing the 30 most differentially expressed DC ligands (Fig. 8f). Overall, in the OCDC + NRT group, DCs exhibited stronger antigen-presenting ability and promoted T-cell activation and proliferation (Fig. 8f). Through multiplex fluorescence immunohistochemistry detection, we also found that the OCDC + NRT group had more DCs infiltration (Fig. 8g).

We next examined M1-like macrophages with proinflammatory features and M2-like macrophages with anti-inflammatory features in the different groups and found that there were more M1-like macrophages and fewer M2-like macrophages in the OCDC + NRT group (Supplementary Fig. 22a-c). We also performed flow cytometry to detect the macrophages in the splenic lymphocytes and TME of each group. Compared to the control group, the OCDC + NRT group exhibited an increase in M1-like macrophages and a significant decrease in M2-like macrophages within the splenic lymphocytes (Supplementary Fig. 22d, e). In the TME, there was a noticeable increase in M1-like macrophages in the OCDC + NRT group (Fig. 8h and Supplementary Fig. 22f). We further found that the OCDC + NRT group had a higher number of M1-like macrophages in the TME through multi-fluorescence immunohistochemistry detection (Fig. 8i). These results are similar to our ScRNAseq findings. Together, these data showed important correlations between therapeutic approaches and the abundance of specific myeloid cell types. The OCDC vaccine combined with adoptive NRT recruits more activated DCs and M1-like macrophages to the tumor region, thereby establishing a TME conducive to tumor suppression.

The OCDC vaccine combined with adoptive NRT transfer affects the growth of cancer cells

The malignant cells in our samples were reclustered, and 11 new clusters were generated (Fig. 9a and Supplementary Fig. 23a). The distribution of the proportions of different clusters varied among the groups (Fig. 9b), and the heterogeneity of DEGs between clusters was high (Supplementary Fig. 23b). Kyoto Encyclopedia of Genes and Genomes (KEGG) enrichment analysis revealed that genes in the OCDC + NRT cohort were enriched in immune-related pathways, especially TCR-related pathways (Fig. 9c).

By CNV analysis, we found a loss of chromosome 11 and region B (Chr11qB) in the OCDC + NRT group (Fig. 9d and Supplementary Fig. 23c, d), and there were significant differences in the way tumor cells evolved in each group of mice (Fig. 9d and Supplementary Fig. 23c, d). Since these immunogenic neoantigen genes were present mainly on Chr11qB and chromosome 1, we concluded that during the clonal evolution of tumor cells, tumor cells expressing immunogenic neoantigens were targeted and that Chr11qB loss occurred in the OCDC + NRT cohort.

We also noticed that the TF signals were significantly different in the tumor cells among the different groups, indicating that the treatments altered the upstream signals of tumor cell development in unique ways (Supplementary Fig. 23e). Cellular communication analysis revealed specific cellular communication between immune cells and tumor cells in the OCDC + NRT cohort, especially Tnf-mediated communication between T/NK cell subsets and tumor cells (Fig. 9e).

We followed the method proposed by Muyas et al.[48] to perform somatic mutation analysis. The steps are illustrated in Fig. 9f. The statuses of oncogenic driver gene mutations and neoantigen mutations in cancer cells are shown in Fig. 9g. The frequency of neoantigen mutations in cancer cells was significantly reduced in the OCDC + NRT cohort (Fig. 9h). According to the above results, we concluded that the combination of OCDC vaccination with NRT adoptive transfer might affect the growth of tumor cells by altering the TME, and tumor cells expressing neoantigens were indeed targeted directly.

Neoantigen-specific T-cell gene signatures are associated with improved clinical outcomes in human cancers

To explore whether the neoantigen-specific T-cell gene signature is reproducible in human cancers, we first defined a gene signature for neoantigen-specific T cells. We screened the genes that characterize neoantigen-specific T cells by different machine learning algorithms (Fig. 10a). With the use of the top algorithm (mean AUC > 0.85, externally validated AUC > 0.8), we found that three genes (Stap1, Ubn2, and Ifng) were associated with multiple algorithms, and we defined the expression of these 3 genes as a cancer neoantigen-specific T-cell (CNST) score, which can be used to infer the neoantigen-specific T-cell fraction (Fig. 10a). We estimated the CNST score in more than 9000 patients with different types of cancer using The Cancer Genome Atlas (TCGA) database and investigated its correlation with prognosis. We found that a high CNST score was associated with a better prognosis (Fig. 10b–e and Supplementary Fig. 24). In human lung adenocarcinoma (LUAD), the CNST score was high and could predict the prognosis of lung adenocarcinoma patients (Fig. 10f and Supplementary Fig. 24).

Immunomodulators (IMs) are critical for cancer immunotherapy, and numerous IM agonizts and antagonists are currently being
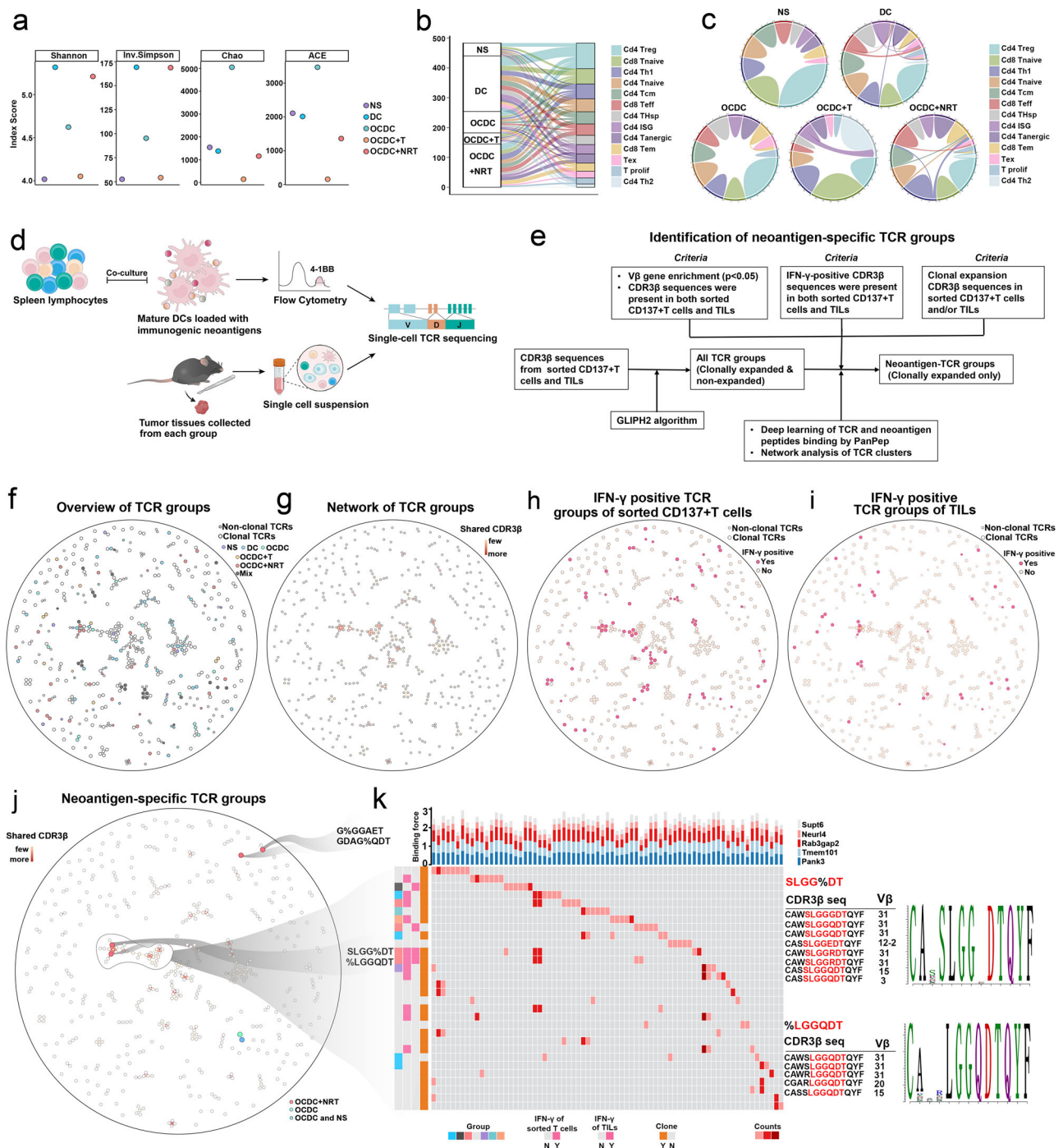
Fig. 5 | Identification of neoantigen-specific TCR groups. a The TCR diversity analysis of different groups included the Shannon index, Inv. Simpson index and richness index (Chao1, ACE) Scores. **b** Sankey diagram showing the proportions of TCRs of each T-cell subtype in the different groups. **c** TCR correlation analysis among T-cell subtypes of different groups. **d** Schematic of single-cell TCR sequencing (scTCR-seq) (Created in BioRender. Min, D. (2024) https://BioRender.com/k17q100). **e** Specificity inference pipeline. **f** Overview of all TCR groups. The size of the dots represents whether the TCR is clonal, large dots represent clonal TCRs, small dots represent nonclonal TCRs, the colors represent TCRs from different groups, and black represents the TCR group originating from two or more groups. **g** The network of the TCR groups. Shared CDR3β sequences organize TCR groups into distinct communities, and the depth of the connecting lines indicates the number of shared CDR3β sequence(s) between any two connected nodes.

h IFN-γ status of sorted CD137 + T cells. Magenta dots represent the IFN-γ-positive TCR groups. (**i**) IFN-γ status of TILs. Magenta dots represent the IFN-γ-positive TCR groups. **j** The neoantigen-specific TCR groups. Red indicates the neoantigen-specific TCR groups originating from the OCDC + NRT cohort. The blue and green colors indicate the neoantigen-specific TCR groups originating from the OCDC group and NS group, respectively. **k** Neoantigen-specific TCR groups and cluster visualization diagrams. One large neoantigen-related community is circled, and the CDR3β members of the specificity groups are highlighted with the short motifs "SLGG%DT" and "LGGQDT" in red font; heatmap showing distinct CDR3β members (columns); table showing an example of the "SLGG%DT" and "LGGQDT" specificity groups. The counts of Vβ gene usage are shown. Source data are provided as a Source Data file.
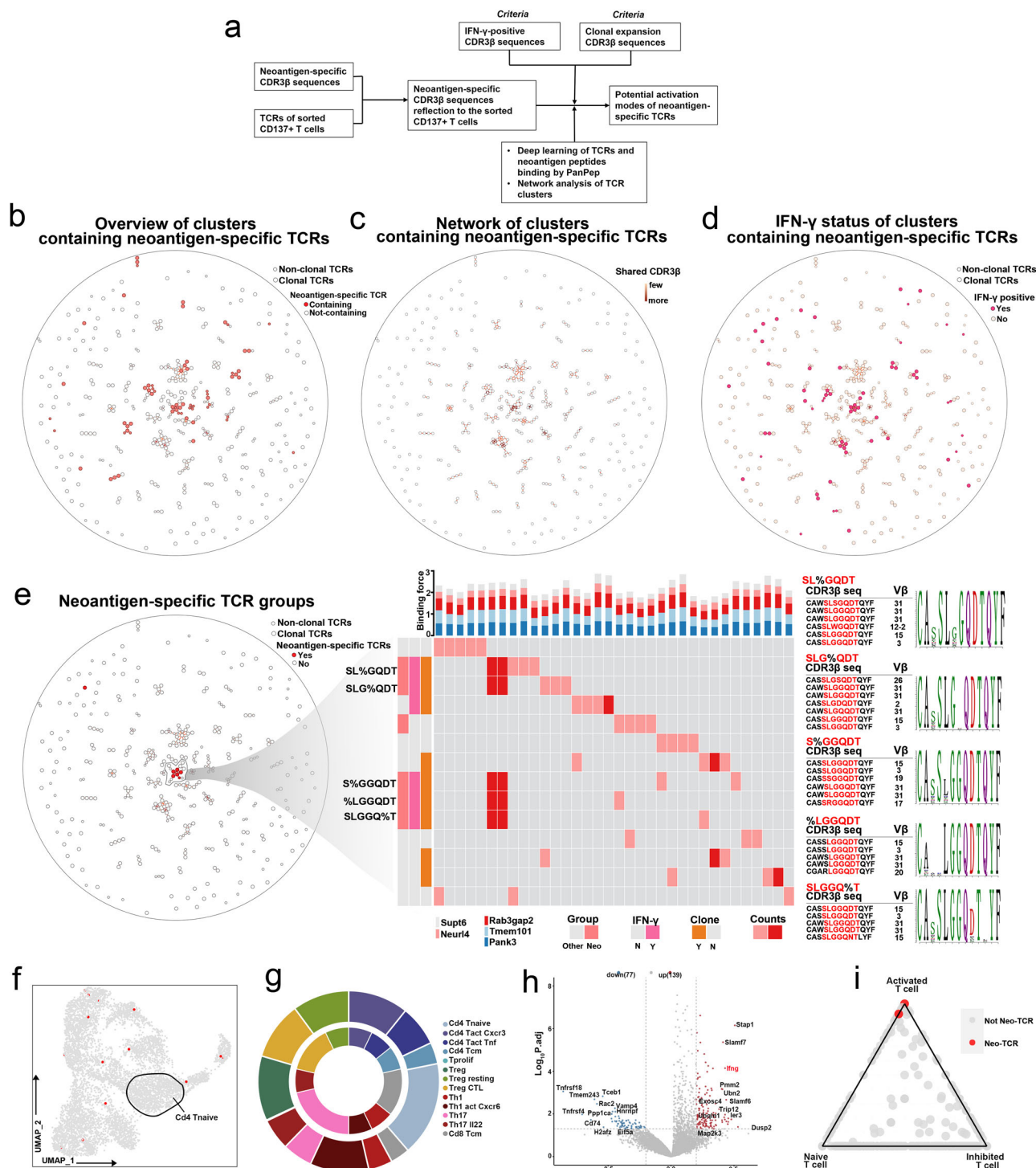
evaluated in clinical oncology research[49]. To advance this research, understanding the expression and regulatory mechanisms of these genes across different CNSTs is needed. We examined IM gene expression, somatic copy number alterations (SCNAs), and expression regulation via epigenetic and mRNA mechanisms. The gene expression patterns of IMs varied across different CNSTs, and the vast majority of IMs, such as antigen presentation-related genes, were expressed in groups with high CNSTs, which is perhaps indicative of the role of the CNST in regulating the TME (Fig. 10g). We also found that the CNST score was positively associated with the infiltration of most immune cell types and was also positively correlated with immune cell infiltration in different cancers (Fig. 10h, i). Thus, the discriminative

markers of mouse neoantigen-specific T cells are predictive of patient survival in patients with high infiltration of immune cell types.

Discussion

ACT therapy using neoantigen-specific T cells is an ideal immunotherapeutic modality. However, due to the low frequency of neoantigen-specific T cells under natural conditions, identifying and screening neoantigen-specific T cells remains a challenge, limiting the widespread development and application of this technology in the clinic[43]. To overcome the above issues, we proposed the strategy of preparing NRTs for adoptive transfer after immunization with a personalized OCDC vaccine. Theoretically, the use of this strategy

Fig. 6 | Characterization of neoantigen-specific T cells. a Specificity inference pipeline. **b** Overview of neoantigen-specific TCR clusters. The size of the dots represents whether the TCR is clonal, large dots represent clonal TCRs, and small dots represent nonclonal TCRs. The red dots represent groups containing neoantigen-specific TCRs. **c** The network of neoantigen-specific TCR clusters. Shared CDR3β sequences organize TCR groups into distinct communities, and the depth of the connecting lines indicates the number of shared CDR3β sequence(s) between any two connected nodes. **d** IFN-γ status of neoantigen-specific TCR clusters. The red dots indicate the IFN-γ-positive TCR groups. **e** The neoantigen-reactive TCR modes. A supercluster containing neoantigen-reactive TCR groups is circled, and the neoantigen-reactive TCR groups are highlighted in red font; the CDR3β members of the neoantigen-reactive TCR groups are highlighted with short motifs; a heatmap showing distinct CDR3β members (columns) of the neoantigen-reactive-related specificity groups (rows) and the counts of shared CDR3β sequences between specificity groups within the circled community; and a table

showing an example of the specificity groups containing the motif (bold). The Vβ gene type is shown. The motif sequence markers corresponding to some motifs are shown on the right. **f** Distribution of T cells containing neoantigen-specific TCRs; red dots indicate that T cells contain neoantigen-specific TCRs. **g** The proportions of neoantigen-specific T cells. The outer circle represents the proportions of different cells among the sorted CD137 + T cells, while the inner circle indicates the proportions of various T cells that contained neoantigen-specific TCRs. **h** Volcano plot showing genes differentially expressed in neoantigen-specific T cells. Each red or blue dot denotes an individual gene passing our *P* value and fold difference thresholds, with red dots indicating genes with upregulated expression and blue dots indicating genes with downregulated expression. Ifng is highlighted in red font. **i** Triangle diagram showing the enrichment of neoantigen-specific T cells in different cells. The red dots indicate the regions where neoantigen-specific T cells are enriched. The *P*-values were analyzed by linear model fit from limma package (**h**). Source data are provided as a Source Data file.

has the following advantages and potential for translation to the clinic.

First, preemptive use of the OCDC vaccine improves the immunosuppressed state of patients, induces neoantigen-specific immune responses, facilitates the preparation of NRT, and prevents the difficult and time-consuming process of identifying and screening neoantigen-specific T cells. Second, OCDC vaccine preparation is easy and fast, and preimmunization with the OCDC vaccine enables patients to receive the vaccine as early as possible, allowing them to buy additional time for subsequent treatments. In addition, the strategy of preparing NRTs for ACT after immunization with the OCDC vaccine is achieved by the combination of both the vaccine and ACT, which is likely to be more effective at treating patients. Our preclinical study supported these hypotheses (Supplementary Fig. 25).

Like the results of Tanyi et al.,[45] our findings confirmed that the OCDC vaccine could improve the immune status of tumor-bearing mice and induce neoantigen-specific immune responses in the TME and splenic lymphocytes. More importantly, NRTs were prepared by using DCs loaded with immunogenic neoantigen peptides cocultured with splenic lymphocytes from mice immunized with the OCDC vaccine. In contrast, the above phenomena were absent in mice not immunized with the OCDC vaccine, indicating that the enhanced neoantigen-specific immune response was indeed induced by the OCDC vaccine. Analysis via scRNA-seq revealed that the NRTs generated by this method contained activated, clonally expanded T cells that exhibited cytotoxic features. Therefore, we concluded that it was feasible to use OCDC vaccine immunization followed by the preparation of NRTs.

Notably, our scRNA-seq analysis of NRTs predominantly featured CD4 + T cells, overshadowing the presence of CD8 + T cells. This observed bias may have stemmed from the higher ratio of CD4 + T cells within the sorted CD3 + CD137 + T cell pool. Consistent with this, our flow cytometry data indicated that CD8 + T cells constitute a substantial portion of the infused NRTs (Supplementary Fig. 26). Furthermore, we postulate that MHC-I-restricted neoantigens could potentially incite a CD4 + T cell-mediated immune response. This hypothesis was supported by the finding that tumor-bearing mice, following immunization with MHC-I-bound neoantigen peptides, predominantly exhibited CD4 + T cell responses to mutated epitopes[50]. Our earlier clinical study also corroborated this, demonstrating that DCs loaded with MHC-I-binding neoantigens could effectively provoke a CD4 + T cell-specific immune response upon vaccination[35].

Since the OCDC vaccine can enrich neoantigen-reactive T cells, it is theoretically feasible to use DCs loaded with tumor lysate to stimulate lymphocytes after OCDC vaccine immunization for adoptive transfer. However, the effectiveness may be compromised by the dilution of the immunogenic tumor antigens. As reported in the literature[51], we speculate that the ideal immunotherapy approach is to

use tumor lysate vaccines to elicit immune responses against both universal and individual neoepitopes, covering all tumor antigens in a broad-spectrum manner, thereby avoiding the tedious and lengthy process of antigen selection. Then, utilize the time gained during the initial immune phase to characterize and identify potential antigenic epitopes, and analyze the patient's immune response for precise design of personalized neoantigen vaccines or neoantigen T cells. Subsequently, use personalized neoantigen vaccines or neoantigen T cells to precisely enhance and amplify the neoantigen-specific T cell response to achieve superior anti-tumor effects.

It is currently believed that combination treatment is the future trend of immunotherapy[49], and vaccines combined with CPB therapy have been reported in many studies[37,42,49,52]. In a recent study, patients were offered further treatment with ACT of vaccine-primed autologous peripheral blood T cells, followed by OCDC vaccine support in ovarian cancer[53]. It was found that the treatment was safe, and epitope spreading with novel neopeptide reactivities was observed after cell infusion in patients who experienced clinical benefit. However, the use of OCDC vaccines followed by NRT adoptive transfer has not yet been reported. Our results demonstrated that the antitumor effect of the OCDC vaccine combined with NRT adoptive transfer was superior to that of the OCDC vaccine alone. LL/2 tumor-bearing mice treated with the combination treatment exhibited not only slower tumor growth and fewer metastatic nodules in the lungs but also prolonged survival. Because of the simplicity and ease of OCDC vaccine and NRT preparation, this therapeutic strategy is worth exploring in clinical studies.

Moreover, we conducted a mechanistic investigation of the use of the OCDC vaccine combined with NRT. By flow cytometry, scRNA-seq, and multiple fluorescence immunohistochemistry, we found that the infusion of T cells could migrate to the TME, and OCDC vaccination combined with NRT infusion could change the TME of mice, increase the infiltration of activated and functional T cells, and decrease the infiltration of Treg cells. Notably, via scTCR-seq, we found that infused neoantigen-specific T cells could migrate into the TME of mice. By constructing neoantigen-specific TCR-T cells, we demonstrated the ability of neoantigen-specific TCR-T to specifically target tumor cells and exert cytotoxicity in vitro. Additionally, the OCDC vaccine combined with NRT treatment increased the infiltration of active DCs, increased the proportion of M1-like macrophages and decreased the proportion of M2-like macrophages. T cells, DCs, and macrophages in the TME can act on tumor cells and change the development and progression of tumor cells, thus exerting antitumor efficacy. This detailed and comprehensive test not only confirmed the feasibility of this combination therapy but also elucidated the inherent mechanism of combination therapy.

Our single-cell analysis revealed a discriminative gene signature of neoantigen-specific T cells that included three genes: Ifng, Stap1 and Ubn2. This signature can identify clonally expanded T cells in human
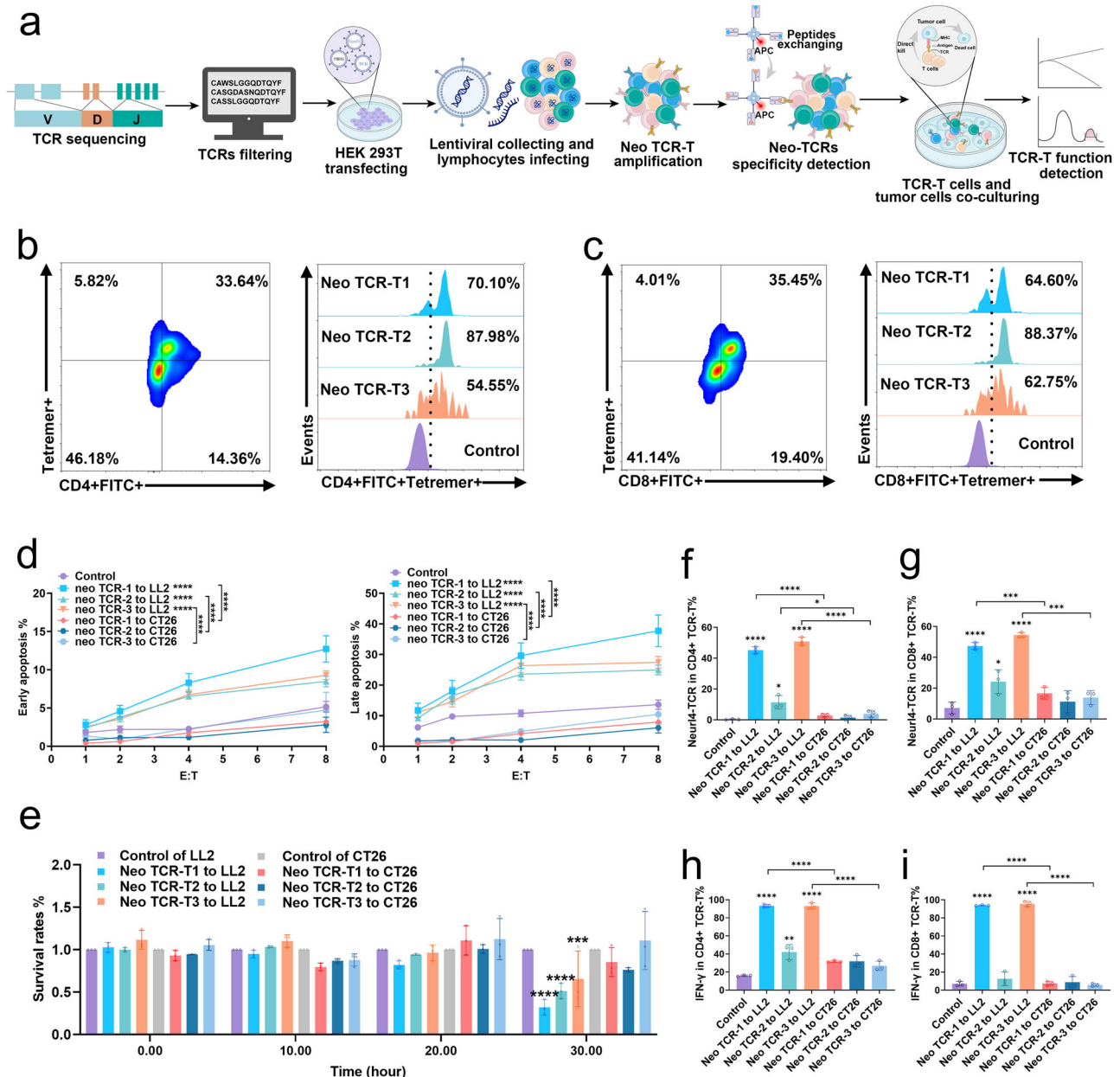
Fig. 7 | Neoantigen-specific TCR-T cells construction and functional validation. **a** Experimental design (Created in BioRender. Min, D. (2024) https://BioRender.com/n63q768). **b** Expression of neoantigen peptide-recognizing TCRs in CD4+ Neo TCR-T cells. **c** Expression of neoantigen peptide-recognizing TCRs in CD8+ Neo TCR-T cells. **d** Apoptotic effects of Neo TCR-T cells on tumor cells ($n = 3$ biologically independent samples). **e** Tumor cells survival rates measured by real-time cell analyzer ($n = 3$ biologically independent samples). **f** Expression of Neurl4 peptide-recognizing TCRs in CD4+ Neo TCR-T cells ($n = 3$ biologically independent samples). **g** Expression of Neurl4 peptide-recognizing TCRs in CD8+ Neo TCR-T cells ($n = 3$ biologically independent samples). **h** Expression of IFN-γ in CD4+ Neo TCR-T cells ($n = 3$ biologically independent samples). **i** Expression of IFN-γ in CD8+ Neo TCR-T cells ($n = 3$ biologically independent samples). Data were expressed as the mean ± SD (**d**–**i**). Two-way ANOVA (**d, e**) and unpaired t test (**f, g, h, i**) were used for statistical analysis, $*p < 0.05$, $**p < 0.01$, $***p < 0.001$ and $****p < 0.0001$. Source data and P values are provided as a Source Data file.

samples and predict patient outcome. Recent studies have reported similar findings confirming that these signature genes are associated with neoantigen-specific T cells[49,54].

Despite these conclusions, we acknowledge the limitations of our current study. First, we prepared NRTs by co-culturing DCs loaded with immunogenic neoantigen peptides with splenocytes from mice immunized with the OCDC vaccine, and therefore the infused cells included T cells and DCs loaded with neoantigens. Further experiments are needed to validate the role of DCs loaded with neoantigens in this system. Second, additional scRNA-seq data from

other qualifying murine models might be needed to verify the signature genes for neoantigen-specific T cells and identify any unknown signature genes. Third, our study focused on analyzing CD137 + T-cell populations in NRTs but excluded other immune cell types. However, our findings suggested that certain myeloid cell populations might also play an important role in combination therapy. Finally, data from clinical studies are needed to verify these conclusions.

We anticipate that the preparation of the NRTs used in this work and the combination treatment of the OCDC vaccine with NRT
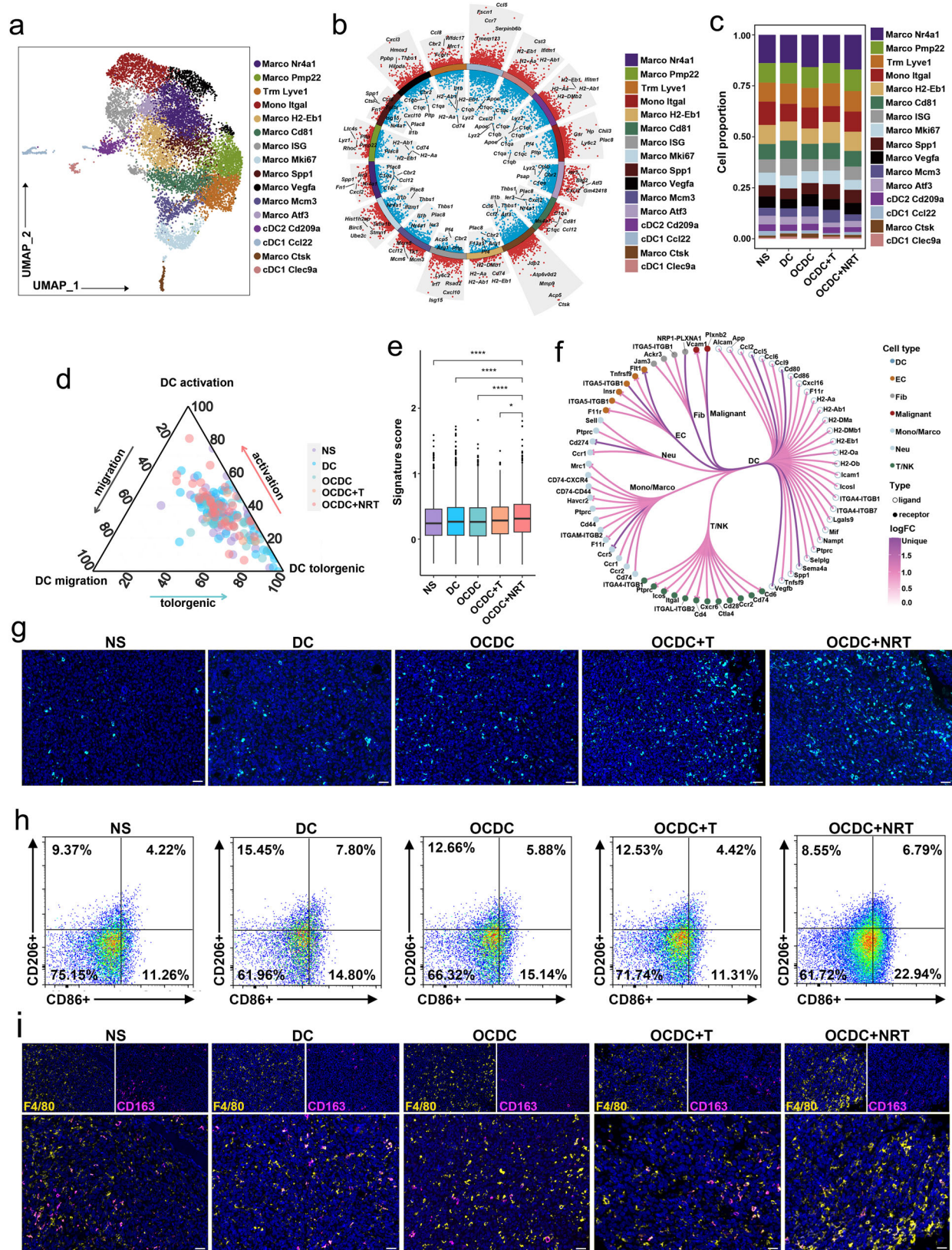
transfer will inform the future development of effective immunotherapy modalities. The biomarkers identified in this work will aid in the future development of effective immunotherapies and provide benefits for predicting the prognosis of cancer patients receiving immunotherapy.

Methods

Mice

Female 6- to 8-week-old C57BL/6 J mice and BALB/C mice were purchased from Beijing HFK Biotechnology Co., Ltd. (Beijing, China), and B6-G/R mice (Strain No. T006163) were purchased from

Fig. 8 | Detection the myeloid cells in the TME. a UMAP plots of myeloid cells, colored by cell type. **b** Circle diagram showing the DEGs in each cell cluster, colored by cell type. **c** Proportions of each cell type in each group, colored by cell type. **d** Triangle plots showing the differences in DC functions in different groups, colored according to group. **e** Box plots showing the enrichment scores of the activated DC signatures across groups (NS: $n = 125$; DC: $n = 174$; OCDC: $n = 136$; OCDC + T: $n = 36$; OCDC + NRT: $n = 123$). **f** Circos plot of the cellular crosstalk between DCs and other cell types in the OCDC + NRT group relative to the remaining groups. The top 30 differentially expressed DC ligands are shown. Pink represents cellular crosstalk that is upregulated in the OCDC + NRT group relative to the remaining groups, and purple represents cellular crosstalk that is specific to the OCDC + NRT group relative to the remaining groups. **g** Representative multiplex fluorescence immunohistochemistry images show DCs in each group ($n = 3$-4 independent fields of view from two independent experiments; scale bar, 20 μm). **h** Representative images showing the proportion of M1-like macrophages and M2-like macrophages within the TME of each group. **i** Representative multiplex fluorescence immunohistochemistry images show M1-like macrophages and M2-like macrophages in each group (F4/80 + CD163- represents like macrophages, and F4/80 + CD163+ represents M2-like macrophages; $n = 3$–4 independent fields of view from two independent experiments; scale bar, 20 μm). The boxes showing the median (horizontal line), second to third quartiles (box), and Tukey-style whiskers (beyond the box) (**e**). Statistical analysis was performed by two-sided Wilcoxon rank-sum test (**e**), *$p < 0.05$, and ****$p < 0.0001$. Source data and P values are provided as a Source Data file.

GemPharmatech Co., Ltd. (Nanjing, China). All mice were maintained under specific pathogen-free conditions, were fed mouse chow and water *ad libitum* and were kept in transparent cages with a controlled temperature (22–24 °C) and light cycle (12 h light, 12 h dark). In our study, the experimental and control animals were co-housed prior to treatment initiation. Once the treatment protocols were defined, the animals were subsequently grouped accordingly and reassigned to separate cages. There were 4-5 mice/cage. This study complied with all relevant ethical regulations and was approved by the Institutional Animal Care and Use Committee of Sichuan University. In the study, once the tumor was visible, the volume of the mouse tumor was measured every 2–3 days. The method for calculating the volume of the mouse tumor was length × width^2/2. The ethics committee allowed a maximum tumor size of 2 cm, and if the maximum size was exceeded, the mouse would be euthanized. In this study, the allowed maximum tumor size was not exceeded. In the study, all mice were euthanized by cervical dislocation. All animal procedures were approved and controlled by the Institutional Animal Care and Treatment Committee of Sichuan University and conducted according to the Animal Care and Use Guidelines of Sichuan University.

Cell lines and cell culture

Mouse Lewis lung carcinoma (LL/2) cell line, colon tumor #26 (CT26) cell line, B16F10 melanoma cell line, and HEK293T cells were obtained from the American Type Culture Collection (ATCC, Manassas, VA, USA). Dulbecco's modified Eagle's medium (DMEM) containing 10% fetal bovine serum (FBS) and 100 units/ml streptomycin and penicillin (PS) was used to culture the LL/2 cells, CT26 cells, B16F10 cells and HEK 293T cells.

Mouse bone marrow-derived dendritic cells (BMDC) were generated from C57BL/6 J female mice according to previous methods[55]. Briefly, bone marrow cells were obtained by flushing the bone marrow cavities of the femur and tibia. After treatment with red blood cell lysis buffer (Solarbio, Beijing, China), the marrow cells were cultured in fresh Roswell Park Memorial Institute (RPMI)-1640 medium supplemented with 10% FBS, 1% PS and 20 ng/ml granulocyte-macrophage colony-stimulating factor (GM-CSF) (Prime Gene Biotechnology, Shanghai, China) for 8 days. On day 3, the medium was replaced with fresh RPMI-1640 medium containing 10% FBS, 1% PS and 20 ng/ml GM-CSF. All cells were cultured at 37 °C in 5% CO2. DMEM, FBS, PS and RPMI-1640 were all purchased from Thermo Fisher Scientific (Waltham, MA, USA).

Whole-exom sequencing, RNA sequencing, and neoantigen analysis

As previously reported[56], 1×10^5 LL/2 cells were subcutaneously implanted on the right back of female C57BL/6 J mice. After 2 weeks, the tumors and whole blood were obtained for DNA and RNA extraction by using a QIAamp DNA Mini Kit (Qiagen) and a QIAamp DNA Blood Mini Kit (Qiagen), respectively. Then, whole-exome sequencing (WES) and RNA sequencing (RNA-seq) were carried out on an Illumina HiSeq-6000 (Illumina, Shanghai, China) performed by Novogene. Co., Ltd (Beijing, China). Based on the sequencing results, mutation calling and neoantigens prediction were performed through the following steps as we described previously[35,57,58]: removal of low-quality reads through a filtering step with fastp[59,60]; WES data: mapping the qualified reads to the mouse reference genome(mm10, C57BL/6 J background) using the BWA-MEM algorithm[61]; detection of variants with Mutect2 following default settings[62]; and mutations were annotated with Variant Effect Predictor (VEP) software, leaving missense mutations; RNA-seq data: clean Fastq files from RNA-seq were aligned to mouse reference genome(mm10) with STAR and the BAM files were subjected for gene quantification using RSEM[63]; estimate the depth of mutations detected by WES in RNA-seq data, leaving mutations with expressed mutated allele; MHC class I affinity was evaluated using the IEDB recommended algorithm (ANN)[64]. Finally, 19 neoantigen candidates were screened out in terms of predicted IC50 (shown in Supplementary Table 1). All the neoantigenic MUT peptides and wild-type (WT) peptides (≥ 98% purity) were synthesized by GL Biochem (Shanghai, China).
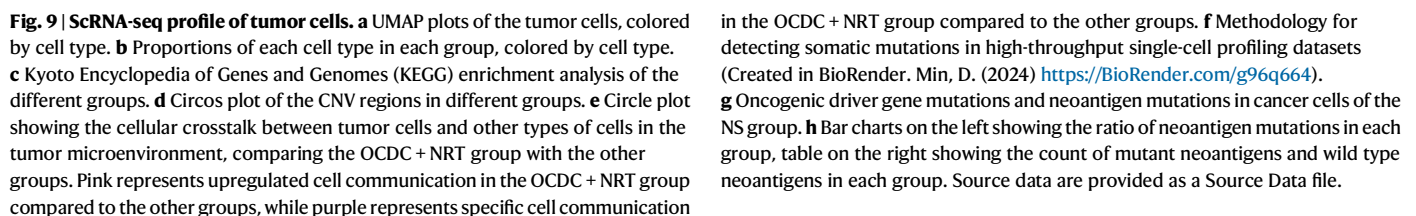
Tumor cell lysate preparation

Tumor lysates were prepared by hypochlorous acid (HOCl) oxidation combined with repeated freeze–thawing[65]. Briefly, a HOCl solution was prepared by diluting the stock NaOCl reagent (Sigma–Aldrich) with Dulbecco's phosphate-buffered saline (DPBS, Corning, USA). The solution was immediately added to the tumor cells to a final density of 1×10^6 cells/ml. The tumor cell suspensions were incubated for 1 h at 37 °C and 5% CO2 with gentle agitation every 30 min to induce oxidation-dependent tumor cell death. Then, these HOCl–oxidized LL/2 cells were frozen at -80 °C for ≥1 h and thawed completely at room temperature 6 times. Trypan Blue (Sigma–Aldrich) staining and an Annexin V-FITC Apoptosis Detection Kit (Beyotime Biotechnology, Shanghai, China) were used to detect the proportion of necrotic cells in tumor lysates from mice treated with different concentrations of HOCl.
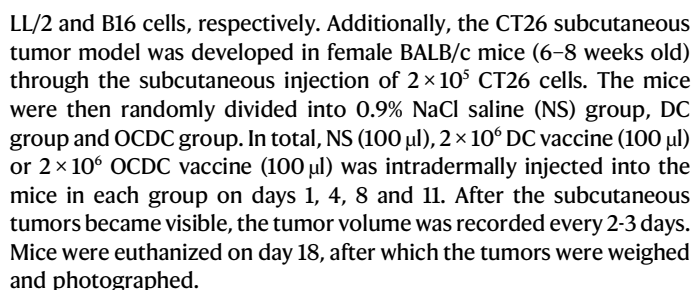
DC vaccine preparation

On day 6 of BMDC induction, tumor lysate-loaded DC vaccines (OCDC vaccines) were prepared with HOCl-oxidized and repeatedly freeze–thawed tumor lysates (DCs to tumor cells were 1:1). Empty-loaded DC vaccines (DC vaccines) were prepared as a control. On day 7, immature DCs were stimulated with lipopolysaccharide (LPS; 1 μg/ml; Beyotime Biotechnology), CpG7909 (10 μg/ml; BrightGene Bio-Medical Technology Co., Ltd, China), and interferon gamma (IFN-γ; 50 ng/ml; Prime Gene Biotechnology) for 24 h to obtain mature DCs. These mature DCs were then harvested, counted and resuspended in phosphate-buffered saline (PBS) or serum-free RPMI-1640 medium for subsequent experiments.

Immunization of subcutaneous tumor model mice

We established the LL/2 and B16 subcutaneous tumor models in female C57BL/6 J mice (6–8 weeks old) by subcutaneously implanting 1×10^5

Fig. 9 | ScRNA-seq profile of tumor cells. a UMAP plots of the tumor cells, colored by cell type. **b** Proportions of each cell type in each group, colored by cell type. **c** Kyoto Encyclopedia of Genes and Genomes (KEGG) enrichment analysis of the different groups. **d** Circos plot of the CNV regions in different groups. **e** Circle plot showing the cellular crosstalk between tumor cells and other types of cells in the tumor microenvironment, comparing the OCDC + NRT group with the other groups. Pink represents upregulated cell communication in the OCDC + NRT group compared to the other groups, while purple represents specific cell communication

in the OCDC + NRT group compared to the other groups. **f** Methodology for detecting somatic mutations in high-throughput single-cell profiling datasets (Created in BioRender. Min, D. (2024) https://BioRender.com/g96q664). **g** Oncogenic driver gene mutations and neoantigen mutations in cancer cells of the NS group. **h** Bar charts on the left showing the ratio of neoantigen mutations in each group, table on the right showing the count of mutant neoantigens and wild type neoantigens in each group. Source data are provided as a Source Data file.

LL/2 and B16 cells, respectively. Additionally, the CT26 subcutaneous tumor model was developed in female BALB/c mice (6–8 weeks old) through the subcutaneous injection of 2×10^5 CT26 cells. The mice were then randomly divided into 0.9% NaCl saline (NS) group, DC group and OCDC group. In total, NS (100 µl), 2×10^6 DC vaccine (100 µl) or 2×10^6 OCDC vaccine (100 µl) was intradermally injected into the mice in each group on days 1, 4, 8 and 11. After the subcutaneous tumors became visible, the tumor volume was recorded every 2-3 days. Mice were euthanized on day 18, after which the tumors were weighed and photographed.

Immunization of lung metastatic tumor model mice

A total of 5×10^5 LL/2 tumor cells were injected into the female C57BL/6 J mice (6–8 weeks old) through the tail vein on day 0. These tumor-bearing mice were randomly grouped into the NS group, DC group and OCDC group. For different treatments, NS (100 µl), 2×10^6 DC vaccine (100 µl) or 2×10^6 OCDC vaccine (100 µl) was intradermally injected into the mice in each group on days 4, 11 and 18 post tumor inoculation. One week after treatment, the mice were euthanized, and the lungs were weighed and photographed.

Fig. 10 | The discriminative marker of neoantigen-specific T cells is associated with improved survival in cancer patients. a Heatmap of the area under the curve (AUC) showing the differences in the ability of the various prediction models to predict neoantigen-specific T cells. **b** Influence of the CNST score on the survival of patients with common cancer types. **c** Kaplan–Meier survival curve for OS in patients with high or low CNST scores. **d** Kaplan–Meier survival curve for progression-free interval (PFI) in patients with high or low CNST scores. **e** Kaplan–Meier survival curve for disease-specific survival (DSS) in patients with high or low CNST scores. **f** CNST scores among cancer types in the TCGA database, ordered by median (ACC: $n = 77$; BLCA: $n = 407$; BRCA: $n = 1091$; CESC: $n = 304$; CHOL: $n = 36$; COAD: $n = 286$; DLBC: $n = 47$; ESCA: $n = 181$; GBM: $n = 159$; HNSC: $n = 518$; KICH: $n = 66$; KIRC: $n = 530$; KIRP: $n = 288$; LAML: $n = 173$; LGG: $n = 510$; LIHC: $n = 369$; LUAD: n = 513; LUSC: $n = 498$; MESO: $n = 87$; OV: $n = 422$; PAAD: $n = 178$; PCPG: $n = 177$; PRAD: $n = 495$; READ: $n = 91$; SARC: $n = 258$; SKCM: $n = 466$; STAD: $n = 414$; TGCT: $n = 132$; THCA: $n = 504$; THYM: $n = 119$; UCEC: $n = 180$; UCS: $n = 57$; UVM: $n = 79$). **g** From bottom to top: mRNA expression (median normalized expression levels); expression versus methylation (gene expression correlation with DNA methylation beta value); amplification frequency (the difference between the fraction of samples in which an IM is amplified in a particular subtype and the amplification fraction in all samples); and deletion frequency (as amplifications) for 66 IM genes by immune subtype. **h** Relationship between the CNST score and infiltration of most immune cells. (**i**) Relationships between CNST scores and immune cell infiltration in patients with different tumors. The boxes showing the median (horizontal line), second to third quartiles (box), and Tukey-style whiskers (beyond the box) (**f**). The P values and hazard ratio (HR) were analyzed by Cox proportional-hazards model (**b**), two-sided log-rank test (**c, d, e**) and Pearson's correlation analysis (**h, i**). Source data and P values are provided as a Source Data file.

Neoantigen reactive T-cell (NRT) preparation

On day 6 of BMDC induction, immature DCs were incubated with the screened immunogenic neoantigen peptide pools (10 µg/ml of each peptide) for 24 h at 37 °C in 5% CO2. After another 24 h of stimulation maturation, the DCs were harvested, washed, resuspended in fresh RPMI-1640 medium free of cytokines at a concentration of 1×10^6 cells/ml, and then cocultured with spleen lymphocytes from mice immunized with the OCDC vaccine for 24 h. The ratio of DCs to lymphocytes was 2:1. Following coculturing, the cells were centrifuged, washed, and resuspended in PBS or RPMI-1640 serum-free medium for adaptive transfer.

DC vaccination and T-cell adaptive transfer combination treatment of subcutaneous tumor model mice

To verify the antitumor effects of the DC vaccine combined with T-cell adaptive transfer in the LL/2 subcutaneous tumor model, female C57BL/6 J mice (6–8 weeks old) were subcutaneously inoculated with 1×10^5 LL/2 tumor cells on day 0. These mice were then randomly divided into the NS group, DC group and OCDC group. There were 12 mice in each group in the NS group and DC group, and 40 mice were in the OCDC group. NS, 2×10^6 DCs and 2×10^6 OCDCs were subcutaneously injected into both sides of the abdomen at 1, 4 and 8 days after tumor inoculation. After vaccination, the OCDC group was randomly divided into the OCDC group, OCDC + T group, and OCDC + NRT group, with 12 mice in each group. After randomization, spleen lymphocytes were obtained from the remaining 4 mice to prepare NRTs. NS, 2×10^6 empty DC-stimulated T cells and 2×10^6 NRTs were injected through the tail vein at 11 and 15 days after tumor inoculation. Tumor volume was recorded every 2 days. Antitumor efficacy was evaluated by determining the tumor growth curve, tumor volume, tumor weight and survival time.

To evaluate the therapeutic effect of the DC vaccine combined with T-cell adaptive transfer in the CT26 and B16 subcutaneous models, 2×10^5 CT26 cells were inoculated in the female BALB/c mice (6–8 weeks old) and 1×10^5 B16 cells in the female C57BL/6 J mice (6–8 weeks old). The dosage and timing of the vaccine and T cell immunization were similar to those of the aforementioned LL/2 subcutaneous model.

DC vaccination and T-cell adaptive transfer combination treatment of LL/2 lung metastasis model

To evaluate the therapeutic efficacy of the DC vaccine combined with T-cell adaptive transfer in the LL/2 lung metastasis model (we also refer to it as the primary tumor model), female C57BL/6 J mice (6–8 weeks old) were injected 2×10^5 LL/2 tumor cells via the tail vein on day 0. These mice were then randomly divided into the NS group, DC group and OCDC group. NS, 2×10^6 DCs and 2×10^6 OCDCs were subcutaneously injected into both sides of the abdomen at 1, 4 and 8 days after tumor inoculation. After vaccination, the OCDC group was randomly divided into the OCDC group, OCDC + T group, and OCDC + NRT group. NS, 2×10^6 empty DC-stimulated T cells and 2×10^6 NRTs were injected through the tail vein at 11 and 15 days after tumor inoculation. One week after treatment, the mice were euthanized, the lungs were photographed, and the tumor nodules were counted.

Safety evaluation

After the mice were euthanized, the main organs were harvested, immediately fixed with 4% paraformaldehyde and then embedded in paraffin. According to the vendor's instructions, the embedded tissue sections were dewaxed and rehydrated before being stained with Mayer's hematoxylin and eosin (H&E) and Masson's trichrome (Solarbio, Beijing, China).

Tetramer preparation

Mutant (MUT) peptides of Pank3, Tmem101, Rab3gap2, Neurl4, and Supt6 were loaded at 10 mM onto the QuickSwitch™ Quant H-2Kb Tetramers-APC (MBL Life Science, Tokyo, Japan) according to manufacturer's instructions. Tetramers were used for staining at 0.2 µM/ml final concentration.

TCR vector construction

Clustering of similar TCR variable region sequences from TCR sequencing results and screening of neoantigen-specific TCR sequences according to clonal amplification and positive IFN-γ expression. TRAV and TRBV were linked to TRAC (GenBank: AAB47020.1, aa 131-268) and TRBC (GenBank: AYL60140.1, aa 138-308), respectively. The TCR Sequences were synthesized as Neo TCR-1, Neo TCR-2 and Neo TCR-3 by GENEVIZ (Suzhou, China). The complete TRA and TRB gene fractions were linked by the P2A connector and constructed into a lentiviral vector (pCDH 2024), which contains a green fluorescent protein (ZGreens) reporter gene.

Lentiviral production

Lentivirus was produced by transfecting HEK 293 T cells with the lentiviral transfer vector. Transfection was performed using the Polyethyleneimine (PEI) according to manufacturer's protocol. Lentiviral supernatants were collected 48 h and 72 h post-transfection and concentrated by polyethylene glycol 8000 (MedChemExpress, HY-Y0873J) and saved at -80 °C or added to T cells.

TCR-T production

Mouse splenic lymphocytes were isolated from C57BL/6 J female mice (6–8 weeks old). After density gradient centrifugation with mouse lymphocyte separation medium (Dakewe, Shenzhen, China) and treatment with red blood cell lysis buffer, murine lymphocytes were activated by 2 ug/ml anti-CD3 antibody (Biolegend, San Diego, USA) and cultured in RPMI-1640 media supplemented with 10% FBS, 1% PS, 50 IU/mL recombinant mouse IL-2 (novoprotein, Suzhou, China), and 2

ug/ml anti-CD28 antibody (Biolegend, San Diego, USA) for 36 h. Then, murine lymphocytes were infected with TCR-expressing lentiviral particles in the presence of 5 µg/ml polypyrene (MedChemExpress, New Jersey, USA). After 24 h post-transfection, fresh RPMI-1640 medium containing recombinant mouse IL-2 and anti-CD28 antibody was added to the cells. TCR-T cells were harvested after 8 days of expansion for quality and functional assessment. The list of antibodies used for T cell expansion is shown in Supplementary Table 2.

Real-Time cell analyzer detection
TCR-T cells cytotoxicity was assayed using a real-time cell analyzer (RTCA) with the xCELLigence system (Agilent, California, USA) according to the manufacturer's instructions. A suspension of 100 µl of LL/2 cells (40,000 cells/well) or CT26 cells (30,000 cells/well) was added to each well. Add 50 µL of suspension containing uninfected T cells T cells or TCR-T cells at an E:T ratio of 4 until the cell index (CI) value ≥ 1. The CI value of each well was automatically monitored by the xCELLigence system for 30 h.

IFN-γ-precoated enzyme-linked immunospot (ELISpot) assay
A mouse IFN-γ precoated ELISpot kit (Dakewe Biotech Co., Ltd., Shenzhen, China) was used to evaluate the neoantigen-specific lymphocyte response. Briefly, to activate the precoated plate, universal serum-free medium for ELISpot (Dakewe Biotech Co., Ltd.) was added for 10 min, after which the wells were emptied by flicking. Splenic lymphocytes ($5\text{-}8 \times 10^4$) from each mouse in the different groups were added to the plate and cultured with 10 µg/ml mutant peptides or wild-type peptides for 20-24 h. Then, the cells were removed, and the plates were washed and incubated with a biotinylated anti-IFN-γ antibody for 1 h at 37 °C. Next, horseradish peroxidase (HRP)-conjugated avidin was added for another hour. Finally, a freshly made 3-amino-9-ethylcarbozole (AEC) chromogenic substrate solution was added for approximately 10-25 min, after which the mixture was washed to terminate the color reaction. Then, the IFN-γ puncta were imaged and counted using an immunospot analyzer/ELISPOT reader (Cellular Technologies Ltd.).

Flow cytometry analysis
Flow cytometry was widely used in this study. For DC vaccine quality testing, mature DCs were harvested, washed and resuspended in PBS. After incubation with CD11c, CD80, and CD86c antibodies at 4 °C in the dark for 40 min, the labeled cells were detected via flow cytometry. For neoantigen-specific response detection, spleen lymphocytes from mice immunized with the OCDC vaccine were cocultured with neoantigen peptide-loaded DCs for 24 h, and the ratio of DCs to lymphocytes was 2:1. Then, the cells were collected and stained with anti-CD3, anti-CD4, anti-CD8, anti-CD134, and anti-CD137 fluorescent antibodies for 40 min, after which the proportion of labeled cells was determined via flow cytometry. For the detection of cytokines, single-cell suspensions from either the spleen or tumor were collected and stained with anti-mouse-CD3, anti-mouse-CD4, or anti-mouse-CD8 antibodies for 40 min. These cells were then fixed, broken, and incubated with anti-mouse IFN-γ, anti-mouse IL-2, and anti-mouse TNF antibodies and subjected to flow cytometry. For the NRTs tracking experiments, mouse splenic lymphocytes or tumor tissues were obtained and stained with Fixable Viability Stain 700 (FVS700) for 10-15 min at room temperature, followed by staining with anti-mouse-CD3 antibody for 40 min, fixation, and permeabilization, and then stained with anti-mouse IFN-γ antibodies for another 40 min. For the detection of immune cells, anti-mouse-CD3, anti-mouse-CD8, and anti-mouse-CD107a or anti-mouse IFN-γ antibodies were used for cytotoxic lymphocytes (CTLs); anti-mouse-CD3, anti-mouse-CD4, anti-mouse-CD25, and anti-mouse-FoxP3 fluorescent antibodies were used for regulatory T cells (Tregs); and anti-mouse-CD3, anti-mouse-CD4, anti-mouse-

CD8, anti-mouse-CD44, and anti-mouse-CD62L fluorescent antibodies were used for memory cells; anti-mouse-CD11b, anti-mouse-F4/80, anti-mouse-CD86 and anti-mouse-CD206 fluorescent antibodies were used for macrophages. For TCR-T cells assays, TCR-T cells and tumor cells were co-cultured at an effector to target cell (E:T) ratio of 4:1 for 48 h. Target cells and TCR-T cells were collected and stained with anti-mouse-CD45, anti-mouse-CD3, anti-mouse-CD4, anti-mouse-CD8, or TCR β antibodies for 40 min. These cells were then fixed, broken, and incubated with anti-mouse IFN-γ antibody and subjected to flow cytometry. For tetramer conjugation assays, TCR-T cells were stained with 0.2 µM/ml H-2Kb tetramer-APC together with anti-mouse-CD45, anti-mouse-CD3, anti-mouse-CD4 and anti-mouse-CD8 antibodies and analyzed by flow cytometry. For apoptosis assay, TCR-T cells were co-cultured at different E:T ratios with different target cell lines for 24 h. Target cells were collected and subjected to flow cytometry using Annexin V-PE/7-AAD Apoptosis Detection Kit (Yeasen Biotechnology (Shanghai) Co., Ltd., shanghai, china). All mouse protein-specific flow cytometry antibodies were listed in the Supplementary Table 3. BD FACS Symphony™ A5, FACS Aria II, and FACS Aria SORP flow cytometers were used to perform fluorescent expression analyzes, and Novo Express software (ACEA Biosciences) and/or FlowJo (FlowJo LLC) software v10.9.0 were used for data analyzes.

Fluorescence-activated cell sorting (FACS) of CD3 + CD137 + T cells
Spleen lymphocytes from mice immunized with the OCDC vaccine were cocultured with screened immunogenic neoantigen peptide-pulsed DCs for 24 h. These cells were subsequently collected and stained with CD3 and CD137 fluorescent antibodies (BD Biosciences, USA) for 40 min, after which the CD3 + CD137 + T cells were sorted via a FACS Aria SORP flow cytometer.

Multiplex immunofluorescence staining
Tumor tissues were immediately harvested from the euthanized mice, fixed with 4% paraformaldehyde and then embedded in paraffin. Four-micron-thick sections cut from the paraffin-embedded blocks were dewaxed in xylene and rehydrated using a decreasing series of ethanol. The as-prepared tumor sections were stained according to the instructions of a six-color multiplex fluorescence immunohistochemical staining kit from Absin Biotech Co., Ltd. (Shanghai, China) or the IRISKit HyperView mIF kit from Luminiris Biotech Co., Ltd. (Chengdu, China). The information on antibodies used in the experiment is provided in Supplementary Table 4, including antibodies against CD3 (Abcam; diluted 1:300), CD3 (Servicebio; diluted 1:1000), CD4 (Abcam; diluted 1:50),CD8 (Abcam; diluted 1:500), CD163 (Servicebio; diluted 1:2000), F4/80 (Servicebio; diluted 1:500), and CD11c (Servicebio; diluted 1:1000). The nuclei were stained with 4',6-Diamidino-2-phenylindole (DAPI) before sealing, and all sections were scanned by a fluorescence imaging camera (Vectra3, Akooya Bioscience, USA).

Frozen section
Immediately after dissecting fresh tumor tissues, they were immersed in 4% paraformaldehyde for fixation for more than 24 h. Then, the fixed tissues were placed in a 15% sucrose solution and dehydrated by sedimentation at 4 °C in a refrigerator. After that, the tissues were transferred to a 30% sucrose solution for further dehydration by sedimentation at 4 °C. Once the tissues were well-dehydrated, optimal cutting temperature (OCT) compound was applied for rapid freezing and embedding. When the OCT turned white and hard, it was ready for sectioning. The section thickness was set to 6-8 micrometers. Subsequently, the sections were stained with DAPI, and after sealing with an antifade mounting medium (Beyotime), they were observed and photographed using the image analysis system LSM 980 by Carl Zeiss (Oberkochen, Germany).

Preparation of single-cell RNA sequencing (scRNA-seq) libraries and sequencing

scRNA-seq was performed with the 10x Genomics single-cell 5′ V(D)J library platform. The cell suspension was loaded into Chromium microfluidic chips with 30 (v2 or v3, depending on the project) chemicalator and barcoded with a 10× Chromium Controller (10X Genomics). Single-cell gene expression and TCR libraries were generated according to the manufacturer's instructions. RNA from the barcoded cells was subsequently reverse-transcribed, and sequencing libraries were constructed with reagents from a Chromium Single Cell 30 v2 (v2 or v3, depending on the project) reagent kit (10X Genomics) according to the manufacturer's instructions. Sequencing was performed with an Illumina platform (HiSeq 2000 or NovaSeq, on the project) according to the manufacturer's instructions (Illumina).

Quality control of the scRNA-seq data

We applied our previously established pipeline to analyze the scRNA-seq data[66–68]. Briefly, we used FastQC to perform basic statistical analysis of the quality of the raw reads. CellRanger was used to convert the raw base call (BCL) files generated by the Illumina sequencer to FASTQ files. Moreover, 10x Genomics does not recommend additional processing of the sequence. If clean reads were indispensable, then the raw read sequences produced by the Illumina pipeline in FASTQ format were preprocessed through Trimmomatic software, which can be summarized as follows: Low-quality reads were removed by scanning the read with a 4-base wide sliding window, cutting when the average quality per base dropped below 10 (SLIDINGWINDOW: 4:10). Remove trailing low quality or N bases (below quality 3) (version 3). Remove adapters: There are two modes to remove the adapter sequence: a. alignment with the adapter sequence, the number of matching bases were greater than 7 and mismatch=2; b. when read1 and read2 overlapping base scoring greater than 30, removed nonoverlapping portions (ILLUMINACLIP: adapter.fa: 2: 30: 7). Drop reads less than 26 bases long. We discarded those reads that could not form pairs. The remaining reads that passed all the filtering steps were counted as clean reads, and all subsequent analyzes were based on these results. Finally, we used FastQC to perform basic statistical analysis of the quality of the clean reads.

Data processing of scRNA-seq and single-cell TCR sequencing (scTCR-seq) libraries

The Cell Ranger Software Suite v.6.1.2 was used to process the raw sequence data into gene expression profiles. The FASTQ files for each sample were processed with a cell ranger count, which was used for mm10 reference genome alignment, filtering and quantifying the reads. The recovered cell parameter was set at 10,000, which is the expected number of cells for each library. The output files of Cell Ranger for each sample included the feature barcode and gene expression information (in unique molecular identifier (UMI) format). Gene expression data were obtained using cellranger aggr, which performed an intersample normalization and merged the results of all samples into one file to remove potential sample variability. For the scTCR-seq data, TCR reads were aligned to the mm10 reference genome, and TCR annotation was performed using the 10x cellranger vdj pipeline. The clonotype of each T-cell was represented by paired alpha and beta CDR3 sequences.

Unsupervised clustering analysis of the scRNA-seq dataset

The Seurat pipeline[69] was used to analyze the combined expression data. Principal component analysis (PCA) of the scaled data of all 2000 genes was performed. Then, a uniform manifold approximation and projection (UMAP) dimensional reduction was performed based on the first 30 principal components to obtain a two-dimensional projection of the cell states. Clusters were identified using shared nearest neighbor-based clustering based on the same principal components.

We used the function FindClusters (v 3.1.2) for clustering with a resolution ranging from 0.1 to 1.5, leading to 7-35 clusters. Silhouette values were calculated for each resolution. These values were subsequently used to determine the optimal cluster number (k). We selected a resolution of 1 by maximizing the average silhouette coefficient, which produced a total of 25 clusters. After removing low-quality and mixed cell clusters, 25 clusters corresponding to 48447 cells were retained for downstream analyzes.

Identification of cluster-specific genes and annotation of cell clusters

We used the FindAllmakers and FindMarkers functions with a Wilcoxon signed-rank test to identify marker genes. For each cluster, only genes that were expressed by more than 20% of the total cells with an adjusted $P < 0.05$ (Benjamin–Hochberg method) were considered. Each cluster was annotated and manually confirmed based on the expression of well-known cell type-specific marker genes. We also used a set of gene markers collected by us to mark different cell types.

Definition of clonal T cells and consistent clones

If at least two cells shared an identical productive alpha-beta pair, those alpha-beta pairs were defined as clonal TCRs. Clonal T cells were defined as those with clonal TCRs. Consistent clones were defined as T cells that harbored identical TCRs detected in both the sorted CD137 + T cells and matched tumor samples.

Pseudotime trajectory analysis

Single-cell trajectory analysis was performed with the Monocle package (v2.18.0)[70]. The starting subject *CellDataSet class* was created with a normalized expression cells × genes matrix. The DEGs across subclusters were identified by performing the *differentialGeneTest* function and subsequently used as genes to define cell progression. The DDRTree function incorporated in the *reduceDimension* function was applied for data dimension reduction. The cells were then ordered in pseudotime with the *orderCells* function. The trajectory was visualized in two-dimensional space by running the *plot_cell_trajectory* function.

Transcription factor (TF) activity analysis

To measure TF activity, SCENIC[71] was applied to determine gene regulatory networks across cell clusters. Briefly, genes coexpressed with TFs were identified using the runGenie3 function of the *GENIE3* package. The aforementioned coexpressed genes were converted into coexpression modules by running the function *runSCENIC_1_coexNetwork2modules*. Potential direct-binding target gene sets (regulons) were identified using the function *runSCENIC_2_createRegulons* implemented in the *RcisTarget* package. The regulon activity was then scored for each cell by performing the *runSCENIC_3_scoreCells* function in the R package *AUCell*. The AUCell matrices were retrieved for heatmap construction.

Cell–cell communication analysis

We employed CellChat (v 1.1.0), a tool tailored for single-cell transcriptome data, to explore cell–cell communications based on the manually curated repository of interacting ligands and receptors[72]. Briefly, the method infers potential cell–cell interactions based on the expression of interacting ligand–receptor pairs between two clusters. The gene encoding a receptor or ligand included in the downstream analysis should be expressed by more than 30% of cells in a specific cluster. To determine the significance of a ligand–receptor pair between two clusters, a permutation test was performed by randomly assigning the cluster labels of each cell 1000 times. The empirical P value was determined by ranking the average expression of a given ligand and receptor pair in two clusters among the 1000 permutated results.

Neoantigen-specific TCR analysis

The GLIPH2 algorithm was used to establish T-cell-specific groups via the use of CDR3β sequences from scTCR-seq. Briefly, GLIPH2 first exhibited clusters of CDR3β sequences sharing either global or local motifs, as previously described[73]. To call the high-confidence CDR3β groups that shared sequence motifs, we applied multiple statistical measurements, including bias in Vβ gene use, CDR3β length distribution and cluster size. Finally, we obtained 462 specificity groups that formed the basis for further analyzes throughout the study.

Gene set enrichment analysis

The R packages clusterProfiler (v3.18.1) and msigdbr (v7.5.1) were used to perform the enrichment analysis. The pathway gene sets we used were extracted from the online databases Kyoto Encyclopedia of Genes and Genomes (KEGG), Gene Ontology (GO), Reactome and curated Hallmark[74]. Pathways were considered enriched if the Benjamini–Hochberg-adjusted false discovery rate (FDR) was <0.05, and the normalized enrichment scores were calculated to represent the enrichment level. Moreover, we scored the gene sets using the gene set variation analysis (GSVA) package (v1.38.2).

Estimation of copy number variation (CNV) in cancer cells

In this study, the InferCNV package was used to analyze cellular CNVs to detect chromosomal amplification or deletion in somatic cells. Due to the properties of the algorithm and the depth limitations of scRNA-sq, the CNVs inferred by this analysis were either whole chromosomes or variants of larger segments of chromosomes. We used "normal" cells, which are theoretically free of CNV, as a control. In this study, normal immune cells were used as the control group for analyzing gene expression at various locations in the genome of the cells to be examined. The procedure is shown below: Prepare 3 sets of input data: a single-cell sequencing raw expression matrix; a grouping file to mark the classification of normal cells versus cells to be tested; and barcode sequences and a gene or chromosome location file. The "run" function was used to analyze the CNV information of the gene expression values of each cell compared to that of the control cell, after which the copy number deletions or amplifications (gene expression differences) on each chromosome were visualized in the form of a heatmap. The genomes of malignant cells generally exhibit significant CNVs compared to those of normal cells, thus distinguishing tumor cells from normal cells[75].

Detection of somatic mutations in single-cell datasets

We used the SComatic algorithm for somatic mutation analysis[76], and the process can be divided into the following four steps: The binary alignment map (BAM) file containing the sequencing reads for all cell types in a sample was split into cell type-specific BAM files using precomputed cell type annotations. The counts of each base in each cell type at each location in the genome were then recorded in a base counting matrix indexed by cell type and genome coordinates. Compute the beta-binomial test for every cell type and position of the genome. The genotype for each cell at the variant sites was computed. Eventually, through the above steps, we obtained single-nucleotide variants (SNVs) for each cell, and we subsequently identified neoantigen mutations for statistical analysis.

Statistics and reproducibility

All the experimental data analyzes were performed with Prism 9 (GraphPad Software). The log-rank test was used for survival, and the t test, Mann–Whitney test and one/two-way ANOVA were used for the other analyzes. $P < 0.05$ was considered to indicate statistical significance. The data collection and analysis were not performed by a researcher blinded to the conditions of the experiments.

Other statistical analyzes

To uncover the discriminative signatures that can accurately distinguish neoantigen-specific T cells from other T cells, we performed multiple machine learning studies and evaluated the area under the curve (AUC) of each combination for identifying neoantigen-specific T cells and other T cells. We selected the 3 most discriminative markers from the top combination (mean AUC > 0.85, externally validated AUC > 0.8) and defined their GSVA score as the CNST score. The CNST was calculated for > 9000 human tumors from 23 major cancer types with RNA-seq and clinical data in the TCGA database. For each cancer type, patients were divided into high and low CNST score subgroups based on the median CNST score. Survival analyzes were conducted with Kaplan–Meier and Cox proportional hazards regression methods. Survival distributions were compared across groups with the log-rank test. Other statistical analyzes in this work, including Wilcoxon signed-sum, chi-square, odds ratio (OR) and correlation tests and down-sampling, were performed using R v4.2.2. All P values from multiple tests were corrected using the Benjamini–Hochberg method and p.adjust function.

Reporting summary

Further information on research design is available in the Nature Portfolio Reporting Summary linked to this article.

Data availability

The raw and processed scRNA-seq/scTCR-seq data in this study are available through the Gene Expression Omnibus under accession GSE271085 and GSE271086. The TCGA database is available at https://portal.gdc.cancer.gov/. The raw flow cytometry data and image data generated in this study have been deposited in the Zenodo under accession DOI link: https://zenodo.org/records/13910755. All data are included in the Supplementary Information or available from the authors, as are unique reagents used in this Article. The raw numbers for charts and graphs are available in the Source Data file whenever possible. Source data are provided with this paper.

Code availability

R codes used to analyze data and generate figures are available at Github (https://github.com/sdzxzh/scNeoT). The scRNA data were processed using Cell Ranger v.6.1.2 (https://www.10xgenomics.com/) and analyzed with the R package Seurat v.4.0.1 (https://satijalab.org/seurat/). Monocle v2.18.0 (https://github.com/cole-trapnell-lab/monocle-release) was used to investigate the transcriptional and developmental trajectories concerning different CD137+ or CD8 + T cell clusters. GLIPH2 algorithm was implemented to identify TCR specificity (http://50.255.35.37:8080/). The R packages clusterProfiler v3.18.1 (https://github.com/YuLab-SMU/clusterProfiler) and msigdbr v.7.5.1 (https://github.com/igordot/msigdbr) were used to perform the GSEA. The SComatic algorithm (https://github.com/cortes-ciriano-lab/SComatic.) was used for somatic mutation analysis.

References

1. Hu, Z., Ott, P. A. & Wu, C. J. Towards personalized, tumour-specific, therapeutic vaccines for cancer. *Nat. Rev. Immunol.* **18**, 168–182 (2018).
2. Morad, G., Helmink, B. A., Sharma, P. & Wargo, J. A. Hallmarks of response, resistance, and toxicity to immune checkpoint blockade. *Cell* **184**, 5309–5337 (2021).
3. Ribas, A. & Wolchok, J. D. Cancer immunotherapy using checkpoint blockade. *Science* **359**, 1350–1355 (2018).
4. Restifo, N. P., Dudley, M. E. & Rosenberg, S. A. Adoptive immunotherapy for cancer: harnessing the T cell response. *Nat. Rev. Immunol.* **12**, 269–281 (2012).

5. Rosenberg, S. A. & Restifo, N. P. Adoptive cell transfer as personalized immunotherapy for human cancer. *Science* **348**, 62–68 (2015).

6. Coulie, P. G., Van Den Eynde, B. J., Van Der Bruggen, P. & Boon, T. Tumour antigens recognized by T lymphocytes: at the core of cancer immunotherapy. *Nat. Rev. Cancer* **14**, 135–146 (2014).

7. Schumacher, T. N. & Schreiber, R. D. Neoantigens in cancer immunotherapy. *Science* **348**, 69–74 (2015).

8. Blass, E. & Ott, P. A. Advances in the development of personalized neoantigen-based therapeutic cancer vaccines. *Nat. Rev. Clin. Oncol.* **18**, 215–229 (2021).

9. Lang, F., Schrors, B., Lower, M., Tureci, O. & Sahin, U. Identification of neoantigens for individualized therapeutic cancer vaccines. *Nat. Rev. Drug Discov.* **21**, 261–282 (2022).

10. Gubin, M. M. et al. Checkpoint blockade cancer immunotherapy targets tumour-specific mutant antigens. *Nature* **515**, 577–581 (2014).

11. Rizvi, N. A. et al. Cancer immunology. Mutational landscape determines sensitivity to PD-1 blockade in non-small cell lung cancer. *Science* **348**, 124–128 (2015).

12. Hugo, W. et al. Genomic and transcriptomic features of response to anti-PD-1 therapy in metastatic melanoma. *Cell* **165**, 35–44 (2016).

13. Riaz, N. et al. Tumor and microenvironment evolution during immunotherapy with nivolumab. *Cell* **171**, 934–949.e16 (2017).

14. Hao, Q. et al. Development and Clinical Applications of Therapeutic Cancer Vaccines with Individualized and Shared Neoantigens. *Vaccines (Basel)* **12**, 717 (2024).

15. Zhou, J., Dudley, M. E., Rosenberg, S. A. & Robbins, P. F. Persistence of multiple tumor-specific T-cell clones is associated with complete tumor regression in a melanoma patient receiving adoptive cell transfer therapy. *J. Immunother.* **28**, 53–62 (2005).

16. Lu, Y. C. et al. Mutated PPP1R3B is recognized by T cells used to treat a melanoma patient who experienced a durable complete tumor regression. *J. Immunol.* **190**, 6034–6042 (2013).

17. Robbins, P. F. et al. Mining exomic sequencing data to identify mutated antigens recognized by adoptively transferred tumor-reactive T cells. *Nat. Med.* **19**, 747–752 (2013).

18. Lu, Y. C. et al. Efficient identification of mutated cancer antigens recognized by T cells associated with durable tumor regressions. *Clin. Cancer Res.* **20**, 3401–3410 (2014).

19. Prickett, T. D. et al. Durable complete response from metastatic melanoma after transfer of autologous T cells recognizing 10 mutated tumor antigens. *Cancer Immunol. Res.* **4**, 669–678 (2016).

20. Yamamoto, T. N., Kishton, R. J. & Restifo, N. P. Developing neoantigen-targeted T cell-based treatments for solid tumors. *Nat. Med.* **25**, 1488–1499 (2019).

21. Tran, E. et al. Cancer immunotherapy based on mutation-specific CD4+ T cells in a patient with epithelial cancer. *Science* **344**, 641–645 (2014).

22. Stevanovic, S. et al. Complete regression of metastatic cervical cancer after treatment with human papillomavirus-targeted tumor-infiltrating T cells. *J. Clin. Oncol.* **33**, 1543–1550 (2015).

23. Tran, E. et al. T-cell transfer therapy targeting mutant KRAS in cancer. *N. Engl. J. Med.* **375**, 2255–2262 (2016).

24. Stevanovic, S. et al. Landscape of immunogenic tumor antigens in successful immunotherapy of virally induced epithelial cancer. *Science* **356**, 200–205 (2017).

25. Zacharakis, N. et al. Immune recognition of somatic mutations leading to complete durable regression in metastatic breast cancer. *Nat. Med.* **24**, 724–730 (2018).

26. Parkhurst, M. et al. Isolation of T-cell receptors specifically reactive with mutated tumor-associated antigens from tumor-infiltrating lymphocytes based on CD137 expression. *Clin. Cancer Res.* **23**, 2491–2505 (2017).

27. Seliktar-Ofir, S. et al. Selection of shared and neoantigen-reactive T cells for adoptive cell therapy based on CD137 separation. *Front. Immunol.* **8**, 1211 (2017).

28. Gros, A. et al. PD-1 identifies the patient-specific CD8+ tumor-reactive repertoire infiltrating human tumors. *J. Clin. Invest.* **124**, 2246–2259 (2014).

29. Yossef, R. et al. Enhanced detection of neoantigen-reactive T cells targeting unique and shared oncogenes for personalized cancer immunotherapy. *JCI Insight* **3**, e122467 (2018).

30. Gros, A. et al. Prospective identification of neoantigen-specific lymphocytes in the peripheral blood of melanoma patients. *Nat. Med.* **22**, 433–438 (2016).

31. Cafri, G. et al. Memory T cells targeting oncogenic mutations detected in peripheral blood of epithelial cancer patients. *Nat. Commun.* **10**, 449 (2019).

32. Cohen, C. J. et al. Isolation of neoantigen-specific T cells from tumor and peripheral lymphocytes. *J. Clin. Invest.* **125**, 3981–3991 (2015).

33. Martin, S. D. et al. A library-based screening method identifies neoantigen-reactive T cells in peripheral blood prior to relapse of ovarian cancer. *Oncoimmunology* **7**, e1371895 (2017).

34. Costa-Nunes, C. et al. High-throughput screening of human tumor antigen-specific CD4 T cells, including neoantigen-reactive T cells. *Clin. Cancer Res.* **25**, 4320–4331 (2019).

35. Ding, Z. et al. Personalized neoantigen pulsed dendritic cell vaccine for advanced lung cancer. *Signal Transduct. Target. Ther.* **6**, 26 (2021).

36. Carreno, B. M. et al. Cancer immunotherapy. A dendritic cell vaccine increases the breadth and diversity of melanoma neoantigen-specific T cells. *Science* **348**, 803–808 (2015).

37. Ott, P. A. et al. An immunogenic personal neoantigen vaccine for patients with melanoma. *Nature* **547**, 217–221 (2017).

38. Sahin, U. et al. Personalized RNA mutanome vaccines mobilize poly-specific therapeutic immunity against cancer. *Nature* **547**, 222–226 (2017).

39. Chen, F. et al. Neoantigen identification strategies enable personalized immunotherapy in refractory solid tumors. *J. Clin. Invest.* **129**, 2056–2070 (2019).

40. Hilf, N. et al. Actively personalized vaccination trial for newly diagnosed glioblastoma. *Nature* **565**, 240–245 (2019).

41. Keskin, D. B. et al. Neoantigen vaccine generates intratumoral T cell responses in phase Ib glioblastoma trial. *Nature* **565**, 234–239 (2019).

42. Ott, P. A. et al. A phase Ib trial of personalized neoantigen therapy plus anti-PD-1 in patients with advanced melanoma, non-small cell lung cancer, or bladder cancer. *Cell* **183**, 347–362.e24 (2020).

43. Li, Q. & Ding, Z. Y. The ways of isolating neoantigen-specific T cells. *Front. Oncol.* **10**, 1347 (2020).

44. Alspach, E. et al. MHC-II neoantigens shape tumour immunity and response to immunotherapy. *Nature* **574**, 696–701 (2019).

45. Tanyi, J. L. et al. Personalized cancer vaccine effectively mobilizes antitumor T cell immunity in ovarian cancer. *Sci. Transl. Med.* **10**, eaao5931 (2018).

46. Kreiter, S. et al. Mutant MHC class II epitopes drive therapeutic immune responses to cancer. *Nature* **523**, 692–696 (2015).

47. Castle, J. C. et al. Exploiting the mutanome for tumor vaccination. *Cancer Res.* **72**, 1081–1091 (2012).

48. Muyas, F. et al. De novo detection of somatic mutations in high-throughput single-cell profiling data sets. *Nat Biotechnol* (2023).

49. Tang, J., Shalabi, A. & Hubbard-Lucey, V. M. Comprehensive analysis of the clinical immuno-oncology landscape. *Ann. Oncol.* **29**, 84–91 (2018).

50. Kreiter, S. et al. Mutant MHC class II epitopes drive therapeutic immune responses to cancer. *Nature* **520**, 692–696 (2015).

51. Harari, A., Graciotti, M., Bassani-Sternberg, M. & Kandalaft, L. E. Antitumour dendritic cell vaccination in a priming and boosting approach. *Nat. Rev. Drug Discov.* **19**, 635–652 (2020).

52. Liu, L. et al. Concurrent delivery of immune checkpoint blockade modulates T cell dynamics to enhance neoantigen vaccine-generated antitumor immunity. *Nat. Cancer* **3**, 437–452 (2022).

53. Bobisse, S. et al. A phase 1 trial of adoptive transfer of vaccine-primed autologous circulating T cells in ovarian cancer. *Nat. Cancer* **4**, 1410–1417 (2023).

54. Awad, M. M. et al. Personalized neoantigen vaccine NEO-PV-01 with chemotherapy and anti-PD-1 as first-line treatment for non-squamous non-small cell lung cancer. *Cancer Cell* **40**, 1010–1026.e11 (2022).

55. Zhang, L. et al. Single-Cell Analyses Inform Mechanisms of Myeloid-Targeted Therapies in Colon Cancer. *Cell* **181**, 442–459.e29 (2020).

56. Kuai, R., Ochyl, L. J., Bahjat, K. S., Schwendeman, A. & Moon, J. J. Designer vaccine nanodiscs for personalized cancer immunotherapy. *Nat. Mater.* **16**, 489–496 (2017).

57. Chen, H. N. et al. Genomic evolution and diverse models of systemic metastases in colorectal cancer. *Gut* **71**, 322–332 (2022).

58. Shu, Y. et al. Prognostic significance of frequent CLDN18-ARHGAP26/6 fusion in gastric signet-ring cell cancer. *Nat. Commun.* **9**, 2447 (2018).

59. Zhang, R. et al. Personalized neoantigen-pulsed dendritic cell vaccines show superior immunogenicity to neoantigen-adjuvant vaccines in mouse tumor models. *Cancer Immunol. Immunother.* **69**, 135–145 (2020).

60. Chen, S., Zhou, Y., Chen, Y. & Gu, J. fastp: an ultra-fast all-in-one FASTQ preprocessor. *Bioinformatics* **34**, i884–i890 (2018).

61. Li, H. & Durbin, R. Fast and accurate long-read alignment with Burrows-Wheeler transform. *Bioinformatics* **26**, 589–595 (2010).

62. Cibulskis, K. et al. Sensitive detection of somatic point mutations in impure and heterogeneous cancer samples. *Nat. Biotechnol.* **31**, 213–219 (2013).

63. Li, B. & Dewey, C. N. RSEM: accurate transcript quantification from RNA-Seq data with or without a reference genome. *Bmc Bioinforma.* **12**, 323 (2011).

64. Andreatta, M. & Nielsen, M. Gapped sequence alignment using artificial neural networks: application to the MHC class I system. *Bioinformatics* **32**, 511–517 (2016).

65. Liu, G. et al. PSSMHCpan: a novel PSSM-based software for predicting class I peptide-HLA binding affinity. *Gigascience* **6**, 1–11 (2017).

66. Luo, H. et al. Pan-cancer single-cell analysis reveals the heterogeneity and plasticity of cancer-associated fibroblasts in the tumor microenvironment. *Nat. Commun.* **13**, 6619 (2022).

67. Mao, W. et al. Pan-cancer single-cell landscape of drug-metabolizing enzyme genes. *Pharmacogenet Genomics* **34**, 217–225 (2024).

68. Zhou, T. et al. The role of long non-coding RNA Maternally Expressed Gene 3 in cancer-associated fibroblasts at single cell pan-cancer level. *Interdiscip. Med.* **2**, e20240018 (2024).

69. Chiang, C. L. et al. A dendritic cell vaccine pulsed with autologous hypochlorous acid-oxidized ovarian cancer lysate primes effective broad antitumor immunity: from bench to bedside. *Clin. Cancer Res.* **19**, 4801–4815 (2013).

70. Butler, A., Hoffman, P., Smibert, P., Papalexi, E. & Satija, R. Integrating single-cell transcriptomic data across different conditions, technologies, and species. *Nat. Biotechnol.* **36**, 411–420 (2018).

71. Qiu, X. et al. Reversed graph embedding resolves complex single-cell trajectories. *Nat. Methods* **14**, 979–982 (2017).

72. Aibar, S. et al. SCENIC: single-cell regulatory network inference and clustering. *Nat. Methods* **14**, 1083–1086 (2017).

73. Jin, S. Q. et al. Inference and analysis of cell-cell communication using CellChat. *Nat. Commun.* **12**, 1088 (2021).

74. Huang, H., Wang, C. L., Rubelt, F., Scriba, T. J. & Davis, M. M. Analyzing the *Mycobacterium tuberculosis* immune response by T-cell receptor clustering with GLIPH2 and genome-wide antigen screening. *Nat. Biotechnol.* **38**, 1194–1202 (2020).

75. Liberzon, A. et al. The molecular signatures database (MSigDB) hallmark gene set collection. *Cell Syst.* **1**, 417–425 (2015).

76. Kurtenbach, S., Cruz, A. M., Rodriguez, D. A., Durante, M. A. & Harbour, J. W. Uphyloplot2: visualizing phylogenetic trees from single-cell RNA-seq data. *BMC Genom.* **22**, 419 (2021).

Acknowledgements

Author contributions

Z.Y.D. and L.Y. designed the study; Q.L., H.Z., T.L. and P.P.W. were responsible for the experiments and writing; T.L. and Q.L. were responsible for the experiments related to TCR-T; R.Z., B.Y.Z., T.F., Y.L.Y., J.M.W., Y.Z., B.L.Z. and Y.S. helped Q.L., H.Z., T.L. and P.P.W. establish the tumor model; and Z.Y.D., H.X. and L.Y. contributed to manuscript corrections. All the authors have read and approved the final manuscript.

Competing interests

The authors declare that they have no competing interests.

Additional information

Supplementary information The online version contains supplementary material available at https://doi.org/10.1038/s41467-024-54650-y.

Correspondence and requests for materials should be addressed to Li Yang or Zhenyu Ding.

Peer review information *Nature Communications* thanks Takashi Morisaki, Kristen Radford and the other, anonymous, reviewer(s) for their contribution to the peer review of this work. A peer review file is available.

Reprints and permissions information is available at http://www.nature.com/reprints